Evaluation of the 3D Near-Surface Velocity Structure in an Urban Environment from Ambient Noise Array Tomography: The Case of the City of Thessaloniki (Northern Greece)

Marios Anthymidis*[1], Costas Papazachos[1], Matthias Ohrnberger[2], Alexandros Savvaidis[3], Nikos Theodoulidis[4], and Dimitris Oikonomou[5]

ABSTRACT

We examine the implementation of ambient noise array tomography in an urban environment to assess the 3D near-surface shear wave velocity (V_S) structure at an intermediate spatial scale ($\sim$1 km^2, depth range 200–300 m). The application employs cross correlation traces of vertical component ambient noise recordings from a local network installed in Thessaloniki city (Northern Greece), allowing the determination of Rayleigh wave travel times for the frequency range of 1.5–14 Hz. The results confirm the presence of a complex subsurface with strong lateral variations in the geology, with travel times varying up to almost one order of magnitude. A surface wave travel time tomography approach was applied for each frequency to determine the spatial variability of the group velocity, involving the use of approximate Fresnel volumes, as well as damping and spatial smoothing constraints to stabilize the results. We also employed an interfrequency smoothing scheme to obtain smooth but data-compatible dispersion curves at the cost of inverting all travel time data simultaneously. Following the application of several quality cutoff criteria, we reconstructed local group slowness dispersion curves for a predefined tomographic grid in the study area. The final 3D velocity model was determined by a modified Monte Carlo inversion of these dispersion curves and the spatial integration of the obtained 1D V_S profiles. Different model parameterizations were tested for the inversion to determine the optimal datafit. The final 3D velocity model is in a very good agreement with the local geology, previous larger scale studies, and other geophysical surveys, providing additional structural constraints (such as hidden fault identification) for the complex sedimentary deposits and bedrock formation in Thessaloniki, up to the depth of $\sim$250–300 m. The introduction of the aforementioned modifications to the ambient noise array tomography suggests that it can be efficiently adjusted and employed as a reliable tool for imaging the 3D seismic structure in urban environments with complex geology.

KEY POINTS

- We show the applicability of ambient noise array tomography in an urban setting, even at small spatial scale.
- The use of Fresnel volumes, interfrequency constraints, and outlier rejection allowed to obtain a robust 3D model.
- Results suggest that ambient noise tomography can be used to reveal unknown 3D features of city geology.

INTRODUCTION

The majority of modern metropolitan areas worldwide are built on sedimentary basins often with relative loose sedimentary deposits that overlay stiffer soil or bedrock formations. In

1. Geophysical Laboratory, Aristotle University of Thessaloniki, Thessaloniki, Greece, https://orcid.org/0000-0001-7408-3070 (CP); 2. Institute of Geosciences, University of Potsdam, Potsdam, Germany, https://orcid.org/0000-0003-1068-0401 (MO); 3. Bureau of Economic Geology, Jackson School of Geoscience, University of Texas at Austin, Austin, U.S.A., https://orcid.org/0000-0001-6373-5256 (AS); 4. Institute of Engineering Seismology and Earthquake Engineering (EPPO-ITSAK), Thessaloniki, Greece, https://orcid.org/0000-0002-0169-9197 (NT); 5. Geophysical-Satellite Remote Sensing and Archaeo-Environment Laboratory (GeoSat ReSeArch), IMS-FORTH, Rethymno, Greece, https://orcid.org/0000-0002-0295-417X (DO)

*Corresponding author: manthymi@geo.auth.gr

Cite this article as Anthymidis, M., C. Papazachos, M. Ohrnberger, A. Savvaidis, N. Theodoulidis, and D. Oikonomou (2022). Evaluation of the 3D Near-Surface Velocity Structure in an Urban Environment from Ambient Noise Array Tomography: The Case of the City of Thessaloniki (Northern Greece), *Bull. Seismol. Soc. Am.* **112**, 2587–2605, doi: 10.1785/0120220004

most cases this type of setting results in complicated wave propagation patterns in the case of major earthquakes with the tendency to intensify the seismic damage potential for strong events (Bard and Bouchon, 1985; Chávez-García and Bard, 1994). These site effects are mainly controlled by the geological formations (stratigraphy, geometry, and geophysical properties), the presence of tectonic features (e.g., faults), as well as their surface topography. Hence, information about the near-surface geophysical structure is essential for seismic risk mitigation and effective urban planning, especially in earthquake-prone areas. More specifically, the shear wave velocity (V_S) distribution with depth is a fundamental property for site response assessment and classification, as well as to a plethora of applications in engineering seismology and geotechnical engineering.

Although borehole data analysis (e.g., crosshole tests) provides accurate local estimates for a variety of geophysical parameters, they often exhibit several shortcomings in urban environments. Their invasive nature, high cost, and localized information limits their use for large-scale or large-depth investigations. The implementation of active geophysical measurements also requires significant effort and is subject to permitting procedures for densely populated cities, whereas in some cases it is simply not possible to ensure reliable data acquisition. For these reasons, alternative approaches have been developed mainly based on the use of ambient noise and earthquake recordings (e.g., Liu *et al.*, 2018; Clayton *et al.*, 2019). These passive methods offer several advantages, such as low costs, minimal requirements of human resources, relatively large penetration depth, and possible implementation at almost any place and time, without causing negative environmental impacts.

The use of ambient noise arrays for the evaluation of 1D V_S models was originally introduced by Aki (1957) with the spatial autocorrelation (SPAC) method. Additional approaches, such as the *f-k* method (Capon, 1969; Lacoss *et al.*, 1969) triggered a large number of studies (e.g., Tokimatsu, 1995; Ohrnberger *et al.*, 2004; Chávez-García *et al.*, 2005; Di Giulio *et al.*, 2006; Köhler *et al.*, 2007; Wathelet *et al.*, 2008; García-Jerez *et al.*, 2010; Anthymidis *et al.*, 2012; Lontsi *et al.*, 2016; Papadopoulos *et al.*, 2017; Martínez-Pagán *et al.*, 2018) focused on determining shallow seismic structure. Practical guidelines were also proposed to improve the reliability of the recovered models (Cornou *et al.*, 2006; Di Giulio *et al.*, 2012; Garofalo *et al.*, 2016; Foti *et al.*, 2017; Hollender *et al.*, 2017). The application of seismic interferometry theory (e.g., Curtis *et al.* 2006) to ambient noise recordings expanded the array technique capability, allowing for 2D and 3D seismic structure imaging. In this approach, a part of the Green's function can be derived by cross-correlating signals of diffuse wavefields obtained from two spatially separated sensors (Chávez-García and Luzon, 2005; Gouédard, Stehly, *et al.*, 2008). Although the diffuse wavefield assumption has been questioned (Mulargia, 2012), it has been shown that ambient noise shows diffuse characteristics if averaged over an adequately long-time period (Shapiro *et al.*, 2005; Pilz and Parolai, 2014). Moreover, the Green's function reconstruction from ambient noise cross correlation was confirmed both experimentally (Campillo and Paul, 2003; Shapiro and Campillo, 2004) and theoretically (Snieder, 2004; Wapenaar *et al.*, 2004; Roux *et al.*, 2005).

The use of ambient noise cross correlation allowed the computation of travel times for the surface waves, as they are dominant in the ambient noise wavefield (Bonnefoy-Claudet *et al.*, 2006), as well as due to their propagation pattern. Hence, travel time tomography can be applied and provide the spatial distribution of group or phase velocity for specific frequencies. However, the generation of 3D V_S models from such group or phase velocity maps is not straightforward. In most cases, local dispersion curves are reconstructed at the tomographic grid nodes, and their 1D inversion leads to the production of the 3D V_S structure. Such ambient noise tomography applications often consider very different spatial scales and environments. For instance, similar methods have been implemented for continental and regional scale for deep crustal studies (Lin *et al.*, 2007; Yang *et al.*, 2007; Saygin and Kennett, 2010; Kao *et al.*, 2013; Goutorbe *et al.*, 2015; Ma and Clayton, 2016) and for very small ones, for example, for material samples with ultrasonic experiments (Lobkis and Weaver, 2001; Derode *et al.*, 2003; Larose *et al.*, 2004; Malcolm *et al.*, 2004; Weaver and Lobkis, 2004).

Ambient noise tomography applications for the near-surface geophysical structure (i.e., tens of meters to few kilometers) have also been performed in nonurban environments or large-scale areas that may include a city complex (Picozzi *et al.*, 2009; Renalier *et al.*, 2010; Pilz *et al.*, 2012; Hannemann *et al.*, 2014; Obermann *et al.*, 2016; Huang *et al.*, 2018; Inzunza *et al.*, 2018). Although in several cases a 3D V_S model is not computed (Nunziata *et al.*, 2009; Huang *et al.*, 2010; Nakata *et al.*, 2011; Lehujeur *et al.*, 2015; Obermann *et al.*, 2015; Pastén *et al.*, 2016; Asano *et al.*, 2017), the results (local 1D V_S models, phase velocity maps, etc.) provide valuable information for several geological problems, for example, geothermal site characterization, deep basin structure, and so on. When a 3D V_S model is computed, this almost always concerns nonurban areas. An impressive example is the pioneering work of Lin *et al.* (2013), in which 3-week noise records from 5200 high frequency (>10 Hz) sensors allowed the recovery of lower frequency Rayleigh dispersion curves (0.4–4 Hz) and the determination of a detailed 3D V_S model, as well as of the Rayleigh wave azimuthal anisotropy for the uppermost crust (~800 m). However, in most cases the spatial (5–40 km) and depth (1–5 km) scales are large, with relatively low resolution (typically >0.5–2 km), focusing on various geological targets such as basin structure, fault mapping, and mining area structure (Xu *et al.*, 2016; Czarny *et al.*, 2019; Taylor *et al.*, 2019; Planès *et al.*, 2020; Zheng *et al.*, 2021).

In the present work, we consider the applicability of ambient noise tomography in the demanding and challenging conditions

of urban areas, where such implementations are rather limited (e.g., Zhou *et al.*, 2021). In most cases, the applications rely on the interpretation of phase velocity maps or inversions for a few 1D local V_S profiles of relatively small scale (depths <10–50 m and spatial extent <50 m; Zhang *et al.*, 2019; Cárdenas-Soto *et al.*, 2020), whereas larger-scale 3D V_S models (e.g., Liang *et al.*, 2019) are often of quite limited resolution and accuracy. The possibility to obtain a reliable 3D near-surface velocity structure in urban environments is critical for a variety of geotechnical and earthquake engineering projects, for example, microzonation studies. Although the application presented in this study concerns an intermediate spatial scale (~1 km^2), it is clearly a reliable solution for urban environments and similar spatial extent, because the implementation of conventional active and passive surveys has to handle two important limitations: (1) For urban settings a large number of local models is required (e.g., 1D V_S models from locally obtained dispersion curves), with an increased cost in time and human resources, and (2) it is often not always feasible to employ high-energy active sources and methods (e.g., seismic refraction, multichannel analysis of surface waves) in densely populated urban environments.

Alternative passive methods performed across linear recording arrays, such as ReMi (Louie, 2001), may fail to correctly determine the low-frequency dispersion characteristics when outline noise sources are stronger than inline noise sources (Xu *et al.*, 2017)—a situation which can be encountered in urban areas. Moreover, passive 1D array techniques (e.g., SPAC) assume a local 1D structure, hence are not suitable in the presence of strong lateral geological–geophysical variations. Ambient noise tomography ameliorates some of the earlier problems. Among others, Gouédard, Comou, and Roux (2008) showed that dispersion curves derived from cross correlations are less affected by the directivity of the ambient noise wavefield, whereas Sager *et al.* (2018) demonstrated that the effect of the noise source distribution on the ambient noise cross correlation travel times and waveform energy is negligible compared to the effect of the actual velocity structure. Further, lateral changes in the subsurface structure can only be identified by a tomographic approach, and additionally the investigation depth is considerably larger compared to both the previously mentioned methods.

The proposed application of ambient noise tomography employs recent and new modifications to the standard procedure, typically followed for the processing of similar noise datasets, allowing its efficient adjustment in urban environments. In particular, we considered Fresnel volumes for the ray paths, thus expanding the influence area of each ray, incorporated interfrequency smoothing constraints in the tomographic inversion, which resulted in smoothed dispersion curves across the tomographic grid nodes and a stabilization of the inversion outcome, utilized an iterative process to reject data outliers, and introduced quantitative cutoff criteria to discard spurious velocity estimations. These modifications allow us to obtain robust V_S models that are compatible with the data and the available geological and geotechnical information for the study area.

The application site is located in the city of Thessaloniki (Northern Greece), close to the city's historical center, including part of the Aristotle University of Thessaloniki campus and the International Exhibition Centre. Within this area we have the transition from the gneiss–greenschist bedrock formations to recent sedimentary deposits (Fig. 1a). According to the previous larger scale surveys in the broader study area (Anastasiadis *et al.*, 2001; Apostolidis *et al.*, 2004; Panou *et al.*, 2005; Skarlatoudis *et al.*, 2010), the bedrock is gradually dipping from this outcrop in the northeast, toward the city's coastline to the southwest, having a roughly 2D geometry, reaching depths that possibly exceed 200 m. The sedimentary deposits overlying the bedrock can be divided into four main lithological units (Anastasiadis *et al.*, 2001; Zervopoulou, 2010); two deeper Neogene age formations superimposed by two more recent, relatively thin Holocene layers. Overall, the stratigraphy (bottom to top) consists of: (1) red clay series, with stiff layers of red silty clays, (2) a sandstone–marl series, comprised of friable to quite compact sandstones, with locally interbedded microconglomerates and marl horizons, (3) a layer of sands, clay, and gravels with a predominance of conglomerates at the base of this sedimentary package, and (4) artificial fill and debris. A typical northeast–southwest cross section in the study area (solid black line in Fig. 1a) is shown in Figure 1c.

DATA ACQUISITION AND APPLICATION OF AMBIENT NOISE ARRAY TOMOGRAPHY IN THE URBAN AREA OF THESSALONIKI CITY

A small circular array of 34 recording stations was installed in the broader area of the Aristotle University campus inside Thessaloniki city (Fig. 1a). All stations were equipped with 24 bit digitizers (200 Hz sampling rate) and three-component broadband sensors (Güralp 6TD and Nanometrics Trillium Compact 120 s coupled with Centaur digitizers), and were temporarily installed mostly inside buildings to reduce the impact of weather and anthropogenic intervention. To minimize soil–structure interaction (SSI) effects on the recorded ambient noise, we avoided large buildings (when possible) and also installed some of the stations in free-field conditions or small buildings (for instance, external hutches used for storage, etc.). It should be noted that because we later determine group and not phase velocities, small or even moderate SSI effects on the ambient noise records is not expected to significantly affect the wavetrain envelope (which is much more robust than, e.g., the phase information), controlling the lag time of coherent surface waves that are recognized by the cross correlation approach later described.

About 14 stations were permanently installed along the outer array circle (diameter of ~900 m) for the whole project duration, whereas 20 temporary stations were moved within

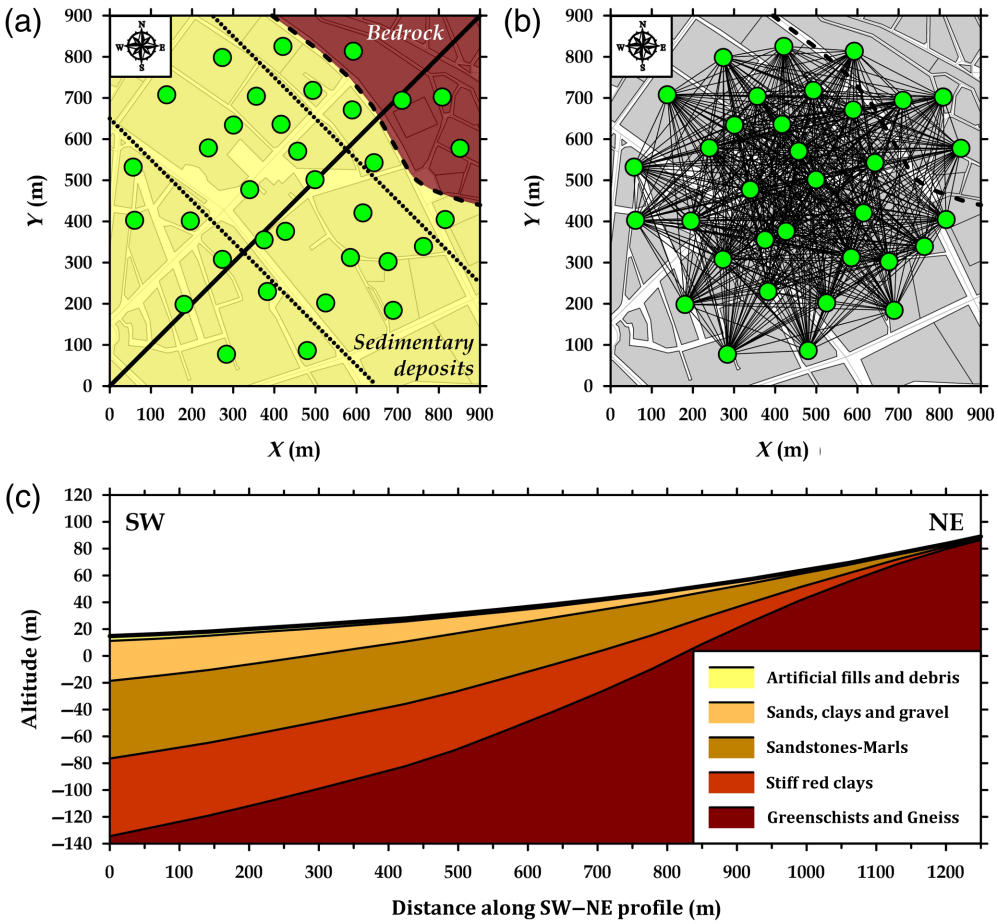

Figure 1. Array geometry and geological information for the study area: (a) geological map and positions of recording stations. The dashed and dotted lines depict the bedrock–sediments contact, and the zone limits later employed for travel time plots, respectively. (b) Ray path coverage of the installed array. (c) Schematic geological cross section along a northeast–southwest profile (solid line in panel a), based on the Anastasiadis *et al.* (2001) model. The color version of this figure is available only in the electronic edition.

the study area in an attempt to realize a rather equidistant distribution. The final geometry involved more than 500 station pairs corresponding to a dense average ray coverage (~10 rays in 100 m^2) of the study area (Fig. 1b), with ray paths of different interstation distances (a few tens to almost 900 m). Because the geology is expected to exhibit significant spatial variability, the array extent ensures the retrieval of V_S information to relatively large depths, that is, 200–300 m. The 14 outer circle stations recorded continuously for almost one month, whereas the temporary stations operated from one to a few days.

As described earlier, the application of ambient noise array tomography involves three main steps: (1) the cross correlation of ambient noise recordings for every station pair to compute Rayleigh wave travel times for different frequencies, (2) a travel time tomography approach to retrieve group slowness maps for the same frequencies and the reconstruction of local group slowness dispersion curves for each node of the tomographic grid, and (3) inversion of these local dispersion curves for the estimation of local 1D V_S profiles for each node, leading to the generation of a 3D V_S model of the subsurface structure from the integration of the 1D profiles, as described in the following.

Cross correlation of ambient noise recordings

We used the vertical records of ambient noise to compute cross correlation traces for Rayleigh waves across all (~560) interstation paths, as Love waves are not observed in vertical components. To obtain robust cross correlations that are not affected by, for example, transient signals (earthquakes, etc.), a suitable data preprocessing was performed following Bensen *et al.* (2007) and Hannemann *et al.* (2014). Cross correlation traces were estimated daily for all the available paths, using 60 s windows with 50% overlap, and stacked to minimize the effect of temporal noise variations (Bensen *et al.*, 2007; Gouédard, Comou, and Roux, 2008; Gouédard, Stehly, *et al.*, 2008). The resulting daily traces were also stacked to produce the final cross correlation trace. The adopted procedure and especially the one-bit normalization proposed by Bensen *et al.* (2007) efficiently reduces the impact of high-amplitude sources, such as traffic noise, which has been shown to be significant in other urban seismic studies (e.g., Inbal *et al.*, 2016; Yang *et al.*, 2021). Moreover, we excluded cross correlation traces with signal-to-noise ratios (SNRs) smaller than 5. To extract Rayleigh wave travel times, we used the multiple filter analysis (Dziewonski *et al.*, 1969), which employs narrow Gaussian band-pass filters, logarithmically spaced in the frequency range of interest (1–50 Hz). The envelope function was calculated for each filtered trace, because its maximum depicts the group-velocity travel time of the Rayleigh waves for the considered frequency. A typical implementation of the multiple filter analysis is illustrated in Figure 2a, in which we can observe the stacked cross correlation trace (on the left) and the filtered traces with their envelope functions.

As illustrated in Figure 2a, the computation of Rayleigh wave travel times often exhibits several problems. The lack

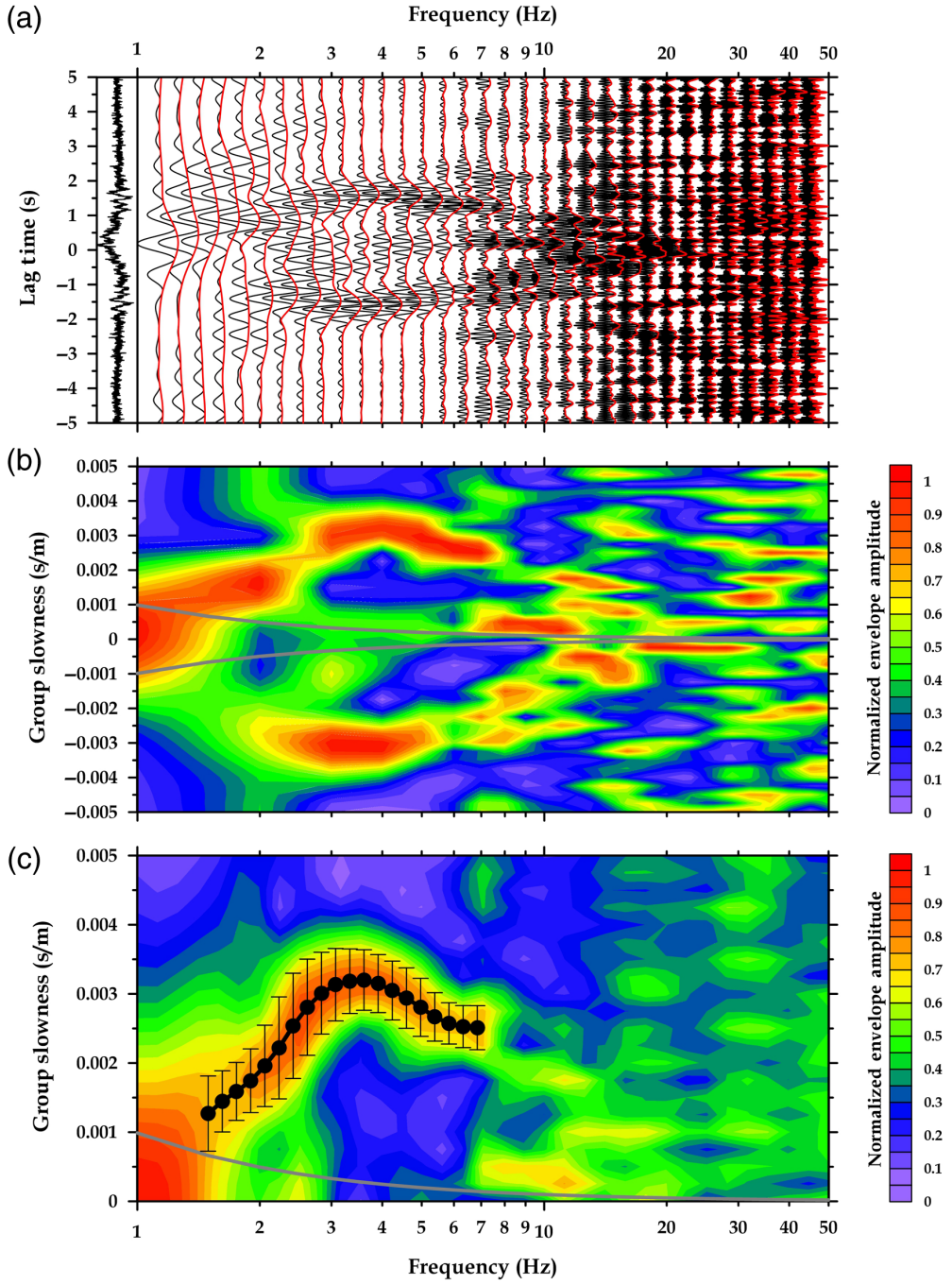

Figure 2. Typical dispersion curve construction procedure: (a) Original (left) and filtered cross correlation traces using narrow Gaussian band-pass filters. Envelope functions for all filtered traces are also plotted. (b) Normalized envelope amplitude distribution against frequency and group slowness generated for the same cross correlation trace. The gray lines depict the low-frequency resolution limit for each path. (c) Root mean square (rms) envelope amplitude distribution determined from the corresponding negative and positive sections shown in panel (b). The manually picked dispersion curve and its uncertainties (black line, with error bars) are also plotted. The color version of this figure is available only in the electronic edition.

of resolution at low frequencies tends to produce flattened envelope functions, making the maximum value detection imprecise. At high frequencies the envelope functions often displayed rather random fluctuations, mainly due to anelastic attenuation and ambient noise scattering. To facilitate the travel time determination, we converted the lag time of the cross correlation traces to group slowness using the known interstation distances for each array station pair, and interpolated the normalized envelope amplitude against frequency and group slowness. An example of the obtained amplitude variation is shown in Figure 2b, in which both negative and positive lag times of the filtered cross correlation traces are shown, corresponding to noise traveling in opposite directions along each interstation path.

To improve the robustness of the picked group slowness dispersion curves, we used the root mean square (rms) amplitude of the corresponding negative and positive slowness sections. The recovered plot (Fig. 2c) was used to pick the group slowness dispersion curves at the observed energy maxima (maximum of envelop functions). The rms stacking makes the maximum energy more pronounced, and the dispersion curve selection becomes straightforward (black line in Fig. 2c). Although manual picking was more time demanding, it allowed to handle complicated patterns such as multibranching (e.g., due to the presence of fundamental and higher modes), gaps, and so on, ensuring the continuity of the picked dispersion curve for the considered frequency range. Moreover, it was possible to then obtain an uncertainty estimate by assigning roughly 1σ-errors when the relative peak amplitude dropped to ~60%, assuming to a Gaussian distribution for the peak rms amplitude. The picked group slowness dispersion curves were logarithmically resampled using 30 frequencies from 1 to 50 Hz. The lower frequency cutoff limit (gray line in Fig. 2c) was estimated from equation $r = 2\lambda_{max}$, in

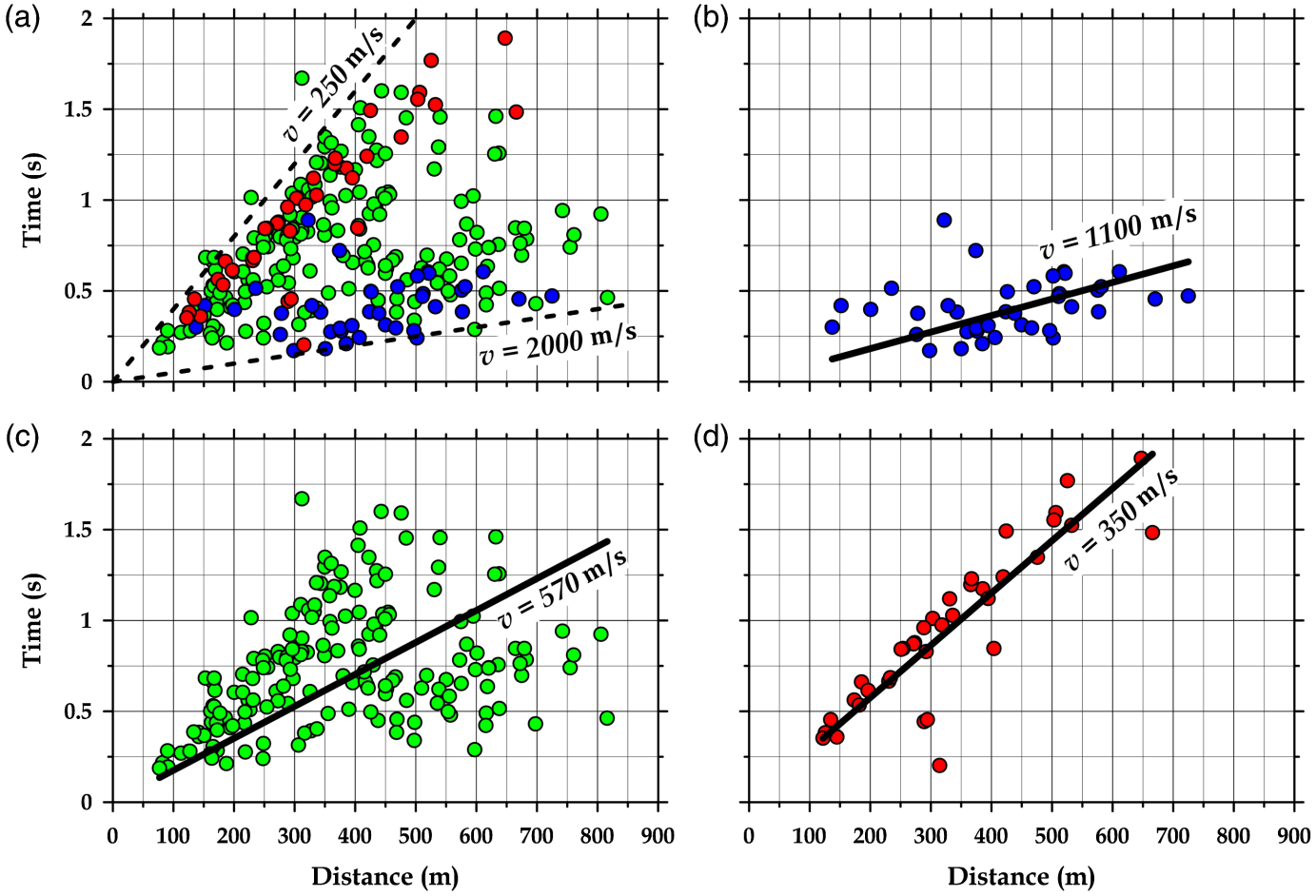

Figure 3. Rayleigh wave group travel time variation with interstation distance for the frequency of 4 Hz in the study area. (a) All data. (b) Paths in the northeast zone of the array (bedrock area, see dotted black lines in Fig. 1a), showing the higher group velocities. (c) Paths crossing the transition zone at the central part of the array. (d) Paths in the southwest part of the array, in which thick sediment deposits are found, showing the lower average group velocities. Indicative minimum and maximum travel time curves are shown in panel (a), whereas least squares, best-fit curves through origin, and the corresponding velocities are shown for panels (b), (c), and (d). The color version of this figure is available only in the electronic edition.

which r is the interstation distance and λ_{max} the maximum recorded wavelength, to ensure that the picked dispersion curves were associated with well-developed Rayleigh waves.

Travel time tomography of Rayleigh waves

The resampled group slowness dispersion curves were converted back to travel times using the interstation distance of each path. Figure 3a shows the complete travel time dataset versus the interstation distance for the frequency of 4 Hz, together with the best fit, running through origin, travel time curves. Although travel times increase with distance, as expected, a rather large data scatter is observed, corresponding to Rayleigh wave group velocities ranging from 250 to 2000 m/s (dashed lines in Fig. 3a). For example, for the interstation distance of 400 m, travel times vary roughly between 0.15 and 1.5 s, practically covering one order of magnitude. These observations reveal the presence of very strong lateral variations in the geology—a rather typical pattern as we move from the fast bedrock outcrop (located in the northeast) toward the southwest (close to Thessaloniki's coastline) where a thickening of the sedimentary formations occurs.

To demonstrate the effect of local geology on travel times, we divided the study area into three zones of northwest–southwest orientation, shown with dotted lines in Figure 1a. The first one covers the northeast part of the array (mainly bedrock outcrop), the second central zone corresponds to the lateral transition from bedrock to the sedimentary formations (that dip to the southwest), and the third zone covers the southwest part of the array, in which thicker, more recent sedimentary deposits are expected. Travel time data were grouped according to their midpath coordinates, and their distribution is shown in Figure 3 for the same frequency (4 Hz). A clear linear trend is seen in the travel time plots both for the northeast (Fig. 3b) and the southwest (Fig. 3d) parts of the study area. An average Rayleigh wave group velocity increase is evident, ranging from ~350 m/s in the sedimentary formations (southwest part) up to ~1100 m/s in the bedrock zone (northeast part). Travel time data from the central transition zone (Fig. 3c) exhibit intermediate group velocities (~570 m/s)

but with much larger variability, showing that the corresponding Rayleigh wavepaths cross a structurally complex transition zone from bedrock to sedimentary layers.

The travel time data for each frequency were used for the determination of group slowness variation in the study area with a tomography approach. Considering the observed travel times, t_1, t_2, …, t_N, from N station pairs and a medium with group slowness, s, the following integral can be used:

$$t_i = \int_{L_i} s dl \quad i = 1, 2, \ldots, N, \tag{1}$$

in which $\boldsymbol{L}$ is the Fermat ray path for the ith station pair. In most cases the group slowness spatial variation is discretized using a tomographic grid of M nodes with slowness, s_j, j = 1, 2, …, M, leading to:

$$\boldsymbol{t} = \boldsymbol{L}\boldsymbol{s}, \tag{2}$$

in which $\boldsymbol{t}$ and $\boldsymbol{s}$ are the travel times and slowness vectors, respectively, and $\boldsymbol{L}$ is an $N \times M$ path lengths matrix. In our case, we used a 900 m × 900 m regular grid of equidistant nodes with a spacing of 100 m. We adopted straight rays for the Rayleigh wave propagation, similar to other studies (Kugler *et al.*, 2007; Pilz *et al.*, 2012; Hannemann *et al.*, 2014), but calculated approximate Fresnel volumes to account for the effect of adjacent grid nodes of the tomographic grid using its simplified geometrical definition proxy for a homogeneous model (Cerveny and Soares, 1992), following Soupios *et al.* (2001). These Fresnel ellipses in our 2D case essentially redistribute the elements of the path length matrix $\boldsymbol{L}$ within each Fresnel ellipse.

To reduce the nonuniqueness and instability typically observed for the least-squares solution of equation (2), several approaches have been proposed (Franklin, 1970; Aki and Lee, 1976; Constable *et al.*, 1987), incorporating damping and smoothing constraints to the linear system of equations. In the present work, we introduced three constraints in equation (2) to produce realistic and robust models for the study area. The first two constraints correspond to conventional damping (for artificial high-amplitude perturbations control) and standard 2D spatially smoothing constraints to regulate the model roughness. The third constraint employed was interfrequency smoothing, which assumes a spatially smoothly varying slowness field not only from node to node (spatial smoothing) but also across neighboring frequencies for the same node of the tomographic grid, following Hannemann *et al.* (2014).

The introduction of these linear constraints to equation (2) was implemented by a damping Lagrangian multiplier (ε) and two Laplacian operators for the spatial (∇^2_{xy}) and interfrequency (∇^2_f) smoothing that were adjusted by additional Lagrangian multipliers λ and μ, respectively. Following these modifications, the linear system of equations to be solved can be written as:

$$\begin{bmatrix} \boldsymbol{t} \\ 0 \\ 0 \\ 0 \end{bmatrix} = \begin{bmatrix} \boldsymbol{L} \\ \lambda\nabla^2_{xy} \\ \mu\nabla^2_f \\ \varepsilon\boldsymbol{I} \end{bmatrix} \boldsymbol{s}. \tag{3}$$

Notice that the employed interfrequency smoothing significantly changes the standard application of travel time tomography. Although equation (2) is usually solved for each frequency, the formulation in equation (3) implies that all travel time data from all the available frequencies are jointly inverted in a single linear system, with the vector $\boldsymbol{s}$ containing the final 2D slowness distribution for all examined frequencies. Although this has certain advantages, later discussed, it is much more computing intensive, especially regarding the memory requirements. The values of the multipliers in equation (3) were determined with a trial-and-error approach. In general, values in the range of 100–300 for the damping, 400–600 for the spatial smoothing, and 800–1200 for the interfrequency smoothing produced comparable and realistic group slowness distributions in the study area. On the contrary, the usage of values outside the aforementioned ranges led either to geophysical models exhibiting strong group slowness variations or oversmoothed distributions of group slowness with significant spatial resolution loss. After parameter trade-off evaluation, we decided to adopt the values of $\varepsilon = 200$, $\lambda = 500$, and $\mu = 1000$, corresponding to the average of the aforementioned ranges.

Equation (3) was solved with conventional least squares to also determine the resolution and covariance matrices, allowing the assessment of the solution quality. Using this information, we computed not only the slowness model error but also the spatial variation of the average resolving length, which quantifies the capability of the available travel time data to identify different spatial scales of group slowness variations (Jackson, 1979; Toomey and Foulger, 1989; Michelini and McEvilly, 1991). To improve the robustness of the model against outliers we solved equation (3) iteratively, employing a data rejection strategy similar to Stehly *et al.* (2006). More specifically, travel time residuals computed from the whole dataset, which exceeded a 2-times standard deviation (residual rms misfit) threshold, were excluded from the next iteration. This 2-standard deviation threshold remained constant during the inversion process. To avoid rejecting large travel time residuals that are actually related to the geophysical structure (e.g., due to the presence of strong velocity anomalies), we allowed all data to be re-examined and used in later iterations, if they fulfilled the rms misfit criterion. In general, after 3 or 4 outlier rejection iterations, the rms of the travel time residuals could not be further reduced.

Figure 4 shows the effect of the iterative data rejection, depicting the variation of the total number of data used, as well as the rms of the travel time residuals against frequency before (first iteration) and after (fourth iteration) data rejection. For the small amount of data at low (1–1.5 Hz) and high (20–40 Hz) frequencies the rejection approach clearly does

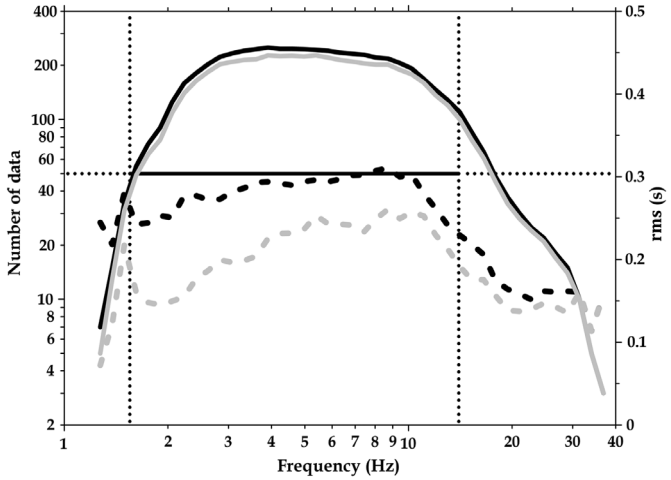

Figure 4. Variation of the total number of data with frequency, before (solid black line) and after (solid gray line) the data rejection procedure. The rms value of the travel time residuals is also presented (dashed black line, no data rejection; dashed gray line, after four iterations and the discarding of large travel time residuals), together with the frequency limits (dotted vertical lines) for which more than 50 data points were available.

not work, because no rms improvement is observed. However, the rms misfit improves when rejection is applied for the frequency range of 2–10 Hz for which more than 100 travel time residuals are available. Even though the data rejection rate after four iterations is not significant (the difference of solid black and gray lines in Figure 4 is rather small, with a maximum outlier rejection rate of 12%), the decrease of the travel time residual rms is rather remarkable, reducing from ∼0.25–0.3 s to ∼0.15–0.2 s on average (dashed black and gray lines in Figure 4, respectively, variance reduction of ∼60%). Based on these results, we limited the tomographic inversion to the frequency range 1.5–14 Hz, for which more than 50 data were available for each frequency.

Although the application of interfrequency smoothing is computationally demanding, as it requires travel time data for all frequencies to be inverted simultaneously in equation (3), its effect on obtaining robust, data-compatible, smooth group slowness dispersion curves is critical. A comparison of local group slowness dispersion curves constructed with and without interfrequency smoothing constraints is shown in Figure 5 for two nodes of the tomographic grid at the southwest (sediments) and the northeast (bedrock) part of the study area. The interfrequency smoothing stabilizes the dispersion curves and minimizes the random fluctuations observed in the case of standard, frequency-independent inversion. We should point out that the interfrequency smoothing applied here differs from typical smoothing methods usually applied posteriori (after inversion) on the dispersion curves, because it is a direct result from the tomographic approach; hence, we obtain smooth dispersion curves that are also compatible with the observed travel time dataset, whereas also minimizing the travel time misfit.

The final group slowness distribution for the study area is presented in Figure 6 for six frequency values (2, 4, 6, 8, 10, and 12 Hz). A similar lateral variation of group slowness can be clearly identified for all frequencies. Low group slowness (high velocities) is observed at the northeast part of the tomographic grid, associated with the presence of the bedrock near the surface. On the contrary, lower velocities are found as we move to the southwest, in which the thickness of the sedimentary deposits is expected to increase. This rapid slowness increase from ∼0.0005 s/m ($V_S \sim 2000$ m/s) in the northeast part of the model to almost ∼0.003 s/m ($V_S \sim 330$ m/s) in the southwest part occurs within a distance of less than 900 m. The spatial pattern of this slowness transition agrees with the northwest–southeast strike of the bedrock–sediments contact, showing an excellent agreement of the results with the available geological information and supporting a rather 2D geometry of the subsurface formations, dipping towards the southwest.

In the results of Figure 6 we can identify two rather problematic areas. More specifically, the bedrock area (northeast part of the model) shows higher slowness (lower velocities) for the frequency of 2 Hz in comparison to higher frequencies, something not expected for a normal V_S increase with depth. A preliminary check of the available data revealed a poor ray path coverage for this frequency in this model section, suggesting that it was not possible to record the very large wavelengths in the bedrock formations for low frequencies with the employed array configuration. Similarly, smaller slowness values (higher velocities) are observed for the frequency of 12 Hz in the southwest part of the model, in comparison to lower frequencies. Again, a poor ray path coverage was identified for this area and frequency, probably due to the strong attenuation of high frequency Rayleigh waves propagating through the low Q_S–low V_S surficial sediments.

To handle these issues generated from poor data coverage, we employed several quality cutoff criteria and discarded group slowness data for nodes that (1) were sampled by less than 50 paths, (2) had relative slowness error larger than 50%, and (3) had resolving length larger than 150 m. The effect of these cutoff criteria on a local group slowness dispersion curve reconstructed from the results of Figure 6 is shown in Figure 7. Although the dispersion curve was originally computed for a wide frequency range (1.3–31 Hz), the final reliable frequency range is much more limited (1.5–9 Hz in this case). It is worth mentioning that the final frequency range is within the limits derived from the iterative data rejection process (Fig. 4).

Following this approach, a total number of 57 local group slowness dispersion curves were finally reconstructed, for different frequency ranges and for each cell of the tomographic grid. In Figure 8, we have plotted all of these curves inside each

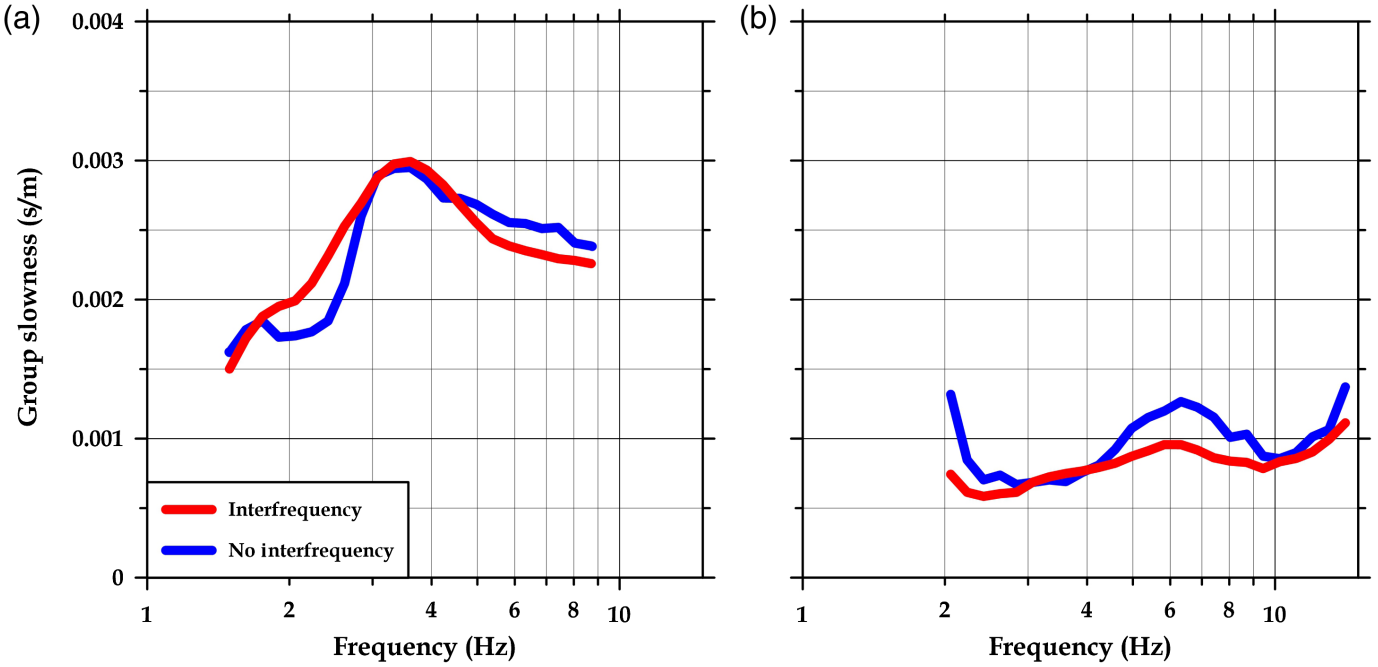

Figure 5. Effect of the interfrequency smoothing constraints on the construction of local dispersion curves for two selected nodes of the tomographic grid. Notice the large group slowness differences between (a) the southwest and (b) the northeast part of the grid. The color version of this figure is available only in the electronic edition.

cell of the tomographic grid. Two important features are clearly noticeable in this figure, namely, the curve shape and the change of the recovered frequency range, respectively, as we move from the southwest to the northeast part of the model. More specifically, a rather clear peak is observed for the dispersion curves in the south-southwest part of the model, indicating a significant velocity impedance contrast at depth in agreement with the significant thickness of sedimentary deposits in this region. Moreover, the frequency range of the dispersion curves is limited to 1.5–9 Hz, mainly due to the attenuation of the high frequency Rayleigh waves propagating through thick sediments that exhibit low V_S and Q_S values (Anastasiadis *et al.*, 2001). On the contrary, flat or nearly flat dispersion curves are observed in the northeast, implying low slowness or high velocities and a relatively homogeneous V_S distribution, associated with the presence of bedrock formations close to or at the surface. Dispersion curves here are not recovered at low frequencies, due to the energy incoherency of the large wavelength surface waves' wavefield, shifting the frequency range to higher frequencies (2–14 Hz) in the broader bedrock area. A transition zone is present at the central part of the model; its narrow spatial extent suggests that the sediments thickness is rapidly changing as we move from northeast to southwest within the study area. It is evident that the employed inversion scheme allowed us to obtain dispersion curves that are robust and reliable for different frequency ranges, depending on the varying effect of the local geology on surface wave propagation (e.g., anelastic attenuation, etc.). As a result, just from the visual inspection of the dispersion curves in Figure 8 and their characteristics (frequency range, shape, etc.), one can easily infer the local geology and expected geophysical structure.

Generation of a 3D shear wave velocity (V_S) model by 1D inversion of dispersion curves

The local dispersion curves were inverted using a modified Monte Carlo approach, namely the neighborhood algorithm (Sambridge, 1999a,b; Wathelet, 2008), as implemented in the software package GEOPSY (Wathelet *et al.*, 2020). This method is a stochastic, direct search inversion technique inside a multidimensional parameter space with irregular boundaries. Its main advantages are its ability to focus the parameter space sampling to geophysical models exhibiting low misfit values and the fast escape from local misfit minima, leading to models with better data fits.

The inversion requires the definition of an appropriate parameter space for the geophysical model, described by the number of layers overlying a half-space, their thickness, as well as the body-wave (P and S) velocities (V_P and V_S, respectively) and density inside each layer. We tested different approaches that might improve the data misfit (i.e., varying number of layers over the half-space, fixed versus widely varying velocities within each layer, velocity gradients, etc.). After several tests, we adopted the ground model parameterization presented in Table 1, which is based on the reference geotechnical model of Anastasiadis *et al.* (2001). In this model, the deep Neogene formation (F) has an average V_S of ~800 m/s and corresponds to the seismic bedrock in the area. The main modification from

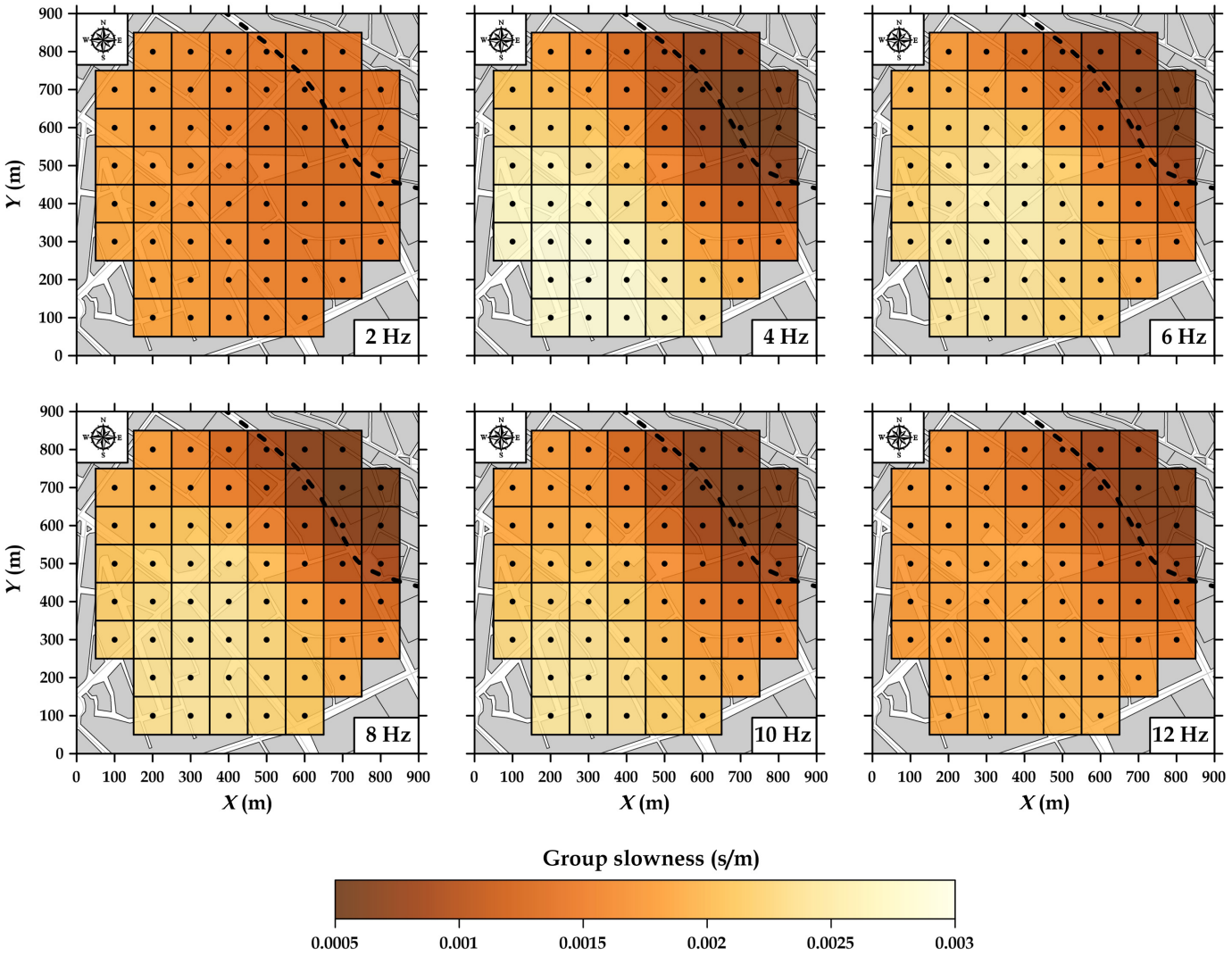

Figure 6. Group velocity maps for six frequencies in the study area. The dashed line indicates the surface contact of bedrock formations and recent sediments. The color version of this figure is available only in the electronic edition.

this model was the adoption of a two-layered bedrock formation (weather bedrock layer G1 and healthy bedrock G in Table 1), as indicated by recent geophysical investigations in the broader bedrock area (e.g., Athanasiou, 2004; Oikonomou, 2017). The V_P and V_S values could vary within the range reported by the reference model of Anastasiadis *et al.* (2001), which has been derived mainly from in-situ geophysical measurements (e.g., crosshole and downhole) and laboratory tests. However, we allowed the layer thickness to vary within wider ranges, considering more recent results (Apostolidis *et al.*, 2004; Panou *et al.*, 2005; Skarlatoudis *et al.*, 2010) that indicated the possible presence of local deviations from the Anastasiadis *et al.* (2001) reference model. Finally, the density of each layer was fixed to the reference model value, because it does not significantly affect the inversion results. It should be noted that the use of a larger number of layers (e.g., two layers for the same geological formation) had the minimal effect on the inversion results, while introducing an unnecessarily more complicated model.

Two examples of 1D V_S profiles from the inversion of the group slowness dispersion curves in the southwest (sediments) and northeast (bedrock) part of the tomographic grid are presented in Figure 9, together with the limits (dashed lines) of the parametric search space, as these are described in Table 1. Because our dispersion curves define the minimum (λ_{min}) and the maximum (λ_{max}) recorded Rayleigh wave wavelength, this imposes specific depth resolution limits to our inversion results. We used the standard quarter-wavelength ($\lambda_{min}/4$) approach (high-frequency limit) for the minimum-depth resolution. Although the low-frequency limit and the maximum depth resolution is not uniform for all dispersion curves, and different limits between λ_{max} and $\lambda_{max}/2$ have been used by various authors for the maximum resolution depth, we adopted the average maximum sensitivity value ($= 0.64\lambda_{max}$) proposed by Pelekis and Athanasopoulos (2011), defined on the basis of a parametric search for a large

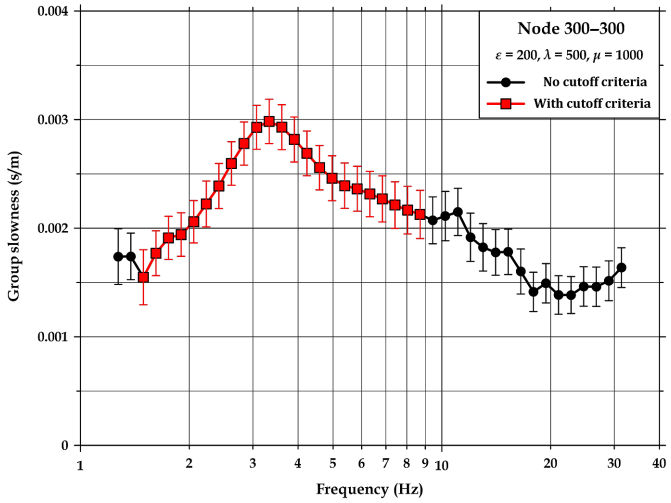

Figure 7. Effect of the cutoff criteria on the reconstruction of local dispersion curves. The frequency range is clearly limited when only the reliable data points are considered (squares with error bars). The color version of this figure is available only in the electronic edition.

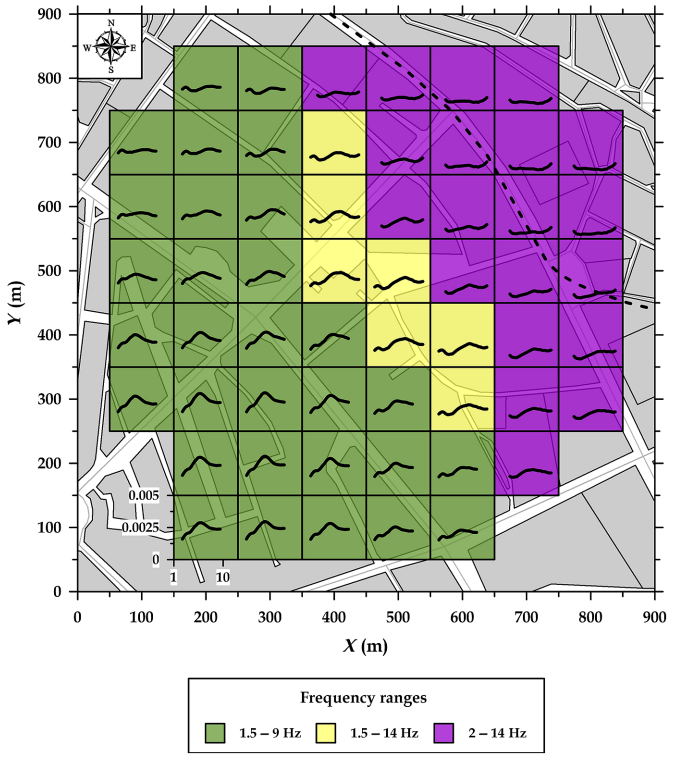

Figure 8. Local group slowness dispersion curves for every tomographic grid node in the study area. A change of the shape and the frequency range is observed as we move from the northeast to the southwest part of the grid. The dashed line indicates the surface contact of bedrock formations and recent sediments. The color version of this figure is available only in the electronic edition.

number of near-surface models. These depth resolution limits are denoted with grayed areas in the corresponding 1D V_S profiles of Figure 9, indicating the part of the model segment that is not well constrained by the data.

The two V_S models presented in Figure 9 show very different features. In the southwest (Fig. 9a) the seismic bedrock depth (E/F contact) occurs at ~70 m, whereas the weathered gneiss bedrock (F/G1 interface) is identified at a much greater depth (~150 m), suggesting a significant sediment thickness in this part of the model. The structure of the surficial layers (A and B) as well as the contact of weathered and healthy bedrock contact (G1/G interface) are not actually constrained by the data, as we have no information in the dispersion curve at very high (>9 Hz) and low frequencies (<1.4 Hz), respectively. On the contrary, the northeast part of the model (Fig. 9b) shows V_S values rapidly increasing from 250 m/s near the surface to almost 1400 m/s at very shallow depths (<25 m). The thickness of all above-bedrock layers is clearly very small (a few meters); however, most formations lie within the unresolved top structure (~15 m), affecting the depth estimation accuracy of the corresponding interfaces. Despite this limitation, the velocity increase from the weathered bedrock layer (G1, $V_S \sim 1400$ m/s) to the healthy bedrock (G, $V_S \sim 2000$ m/s) is adequately constrained.

A 3D V_S model was created by the integration of all 57 minimum-misfit 1D V_S profiles for all tomographic grid nodes. Following the reference model configuration (Table 1), we present in Figure 10 the spatial variation of the lower interface depth for layers that are well resolved, namely E, F, and (partly) G1. Nodes for which the interface depth was ≤10 m (average minimum-depth resolution) or larger than the maximum-

TABLE 1
Ground Model Parameter Space Used for the Inversion of the Local Group Slowness Dispersion Curves

Layer	Geology	Depth Range (m)	V_P (m/s)	V_S (m/s)	Density (kg/m^3)
A	Anthropogenic layer (Holocene)	1–50	400–1700	200–350	2050
B	Soft-to-stiff Quaternary clays and sands	1–100	1350–2350	200–400	2150
E	Stiff Neogene clays	1–250	1500–2500	350–700	2350
F	Stiff-to-very stiff Neogene clays (seismic bedrock)	1–500	2700–3700	700–850	2350
G1	Weathered bedrock	1–500	3500–4500	900–1500	2600
G	Healthy bedrock	Half-space	4000–5000	1500–3000	2600

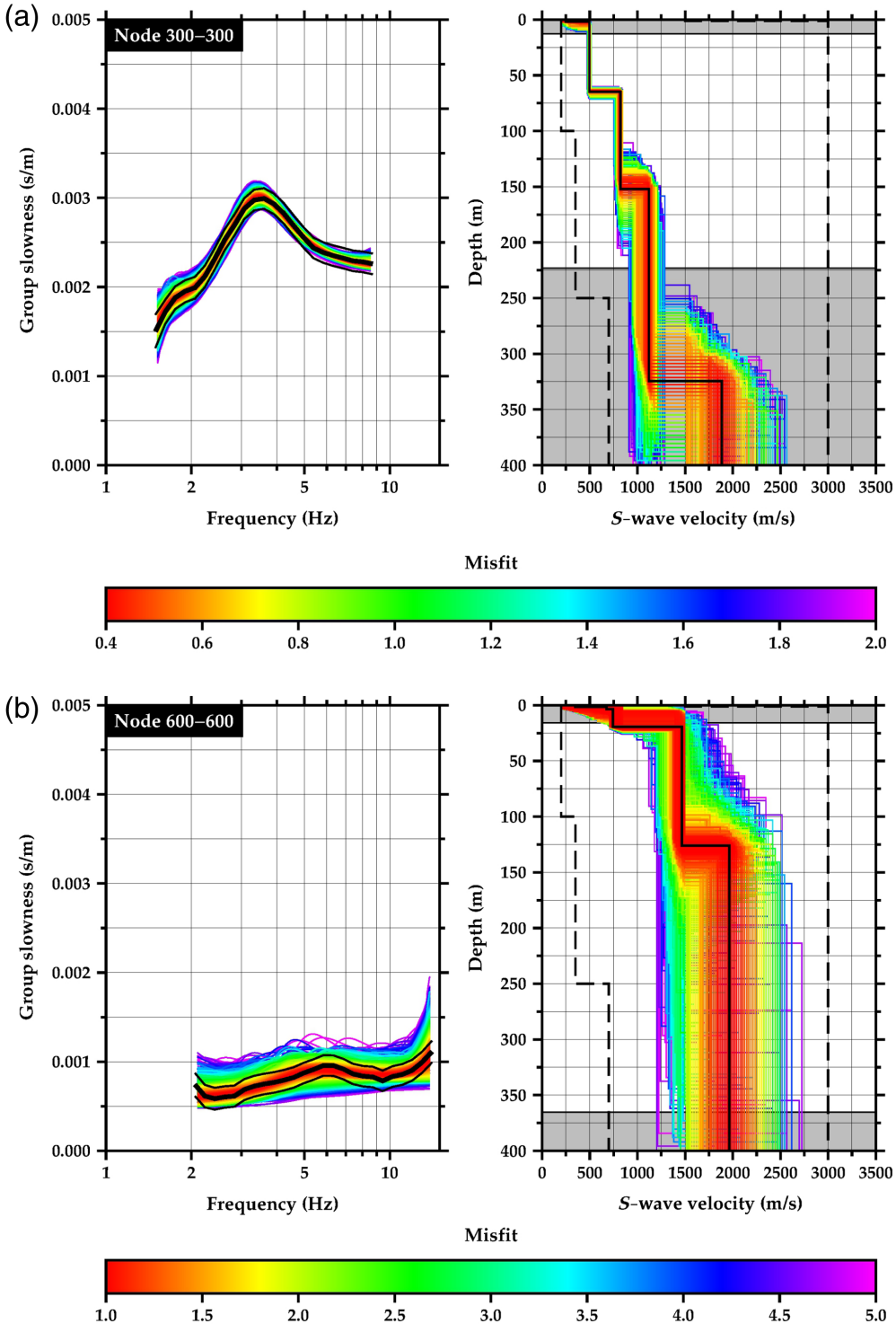

Figure 9. Inversion of two indicative dispersion curves from the (a) southwest and (b) northeast part of the model. Dispersion curves and their standard deviation limits are presented with solid black lines in the left plots. Colored lines in the same plots depict the theoretical dispersion curves for the ground profiles from the Monte Carlo inversion (right plots). The color of each curve is defined by the final relative misfit value (color bars). The grayed areas indicate the depth resolution limits of the models (not constrained by the data), whereas the dashed lines depict the limits of the parameter space explored by the inversion. The color version of this figure is available only in the electronic edition.

depth resolution are depicted with dark colors and a cross symbol, respectively, in the same figure. A 2D geometry is observed for all the interfaces, with layers dipping from northeast toward the southwest, in excellent agreement with the available geological–geotechnical information. Though, for the surficial layers (A and B) we have almost no control on their spatial variation, as we are missing resolution for depths less than ~10 m, we can only determine that their thickness is quite small, certainly less than this average minimum-depth resolution value. The same conclusion can be drawn for the northeast part of the model regarding the deeper Neogene layer E, as well as (to a lesser extent) for the seismic and weathered gneiss bedrock (layers F and G1). Nevertheless, these layers show a clear thickness increase, as we move toward the southwest (toward the city coast), with the strongest increase clearly occurring as we move away from the observed surface sediment-bedrock geological contact (dashed line in Fig. 10). Notice that the obtained depths of the weathered bedrock (G1) in the southwest part of the proposed model are close to or exceeding the maximum depth resolution limit and should be interpreted with caution.

The resolution at larger depths could be improved by the use of information extracted from the horizontal-to-vertical spectral ratio (HVSR) curves of noise records (Nakamura, 1989), which has been proven as a reliable tool for determining the thickness of soft sediments over bedrock (e.g.,

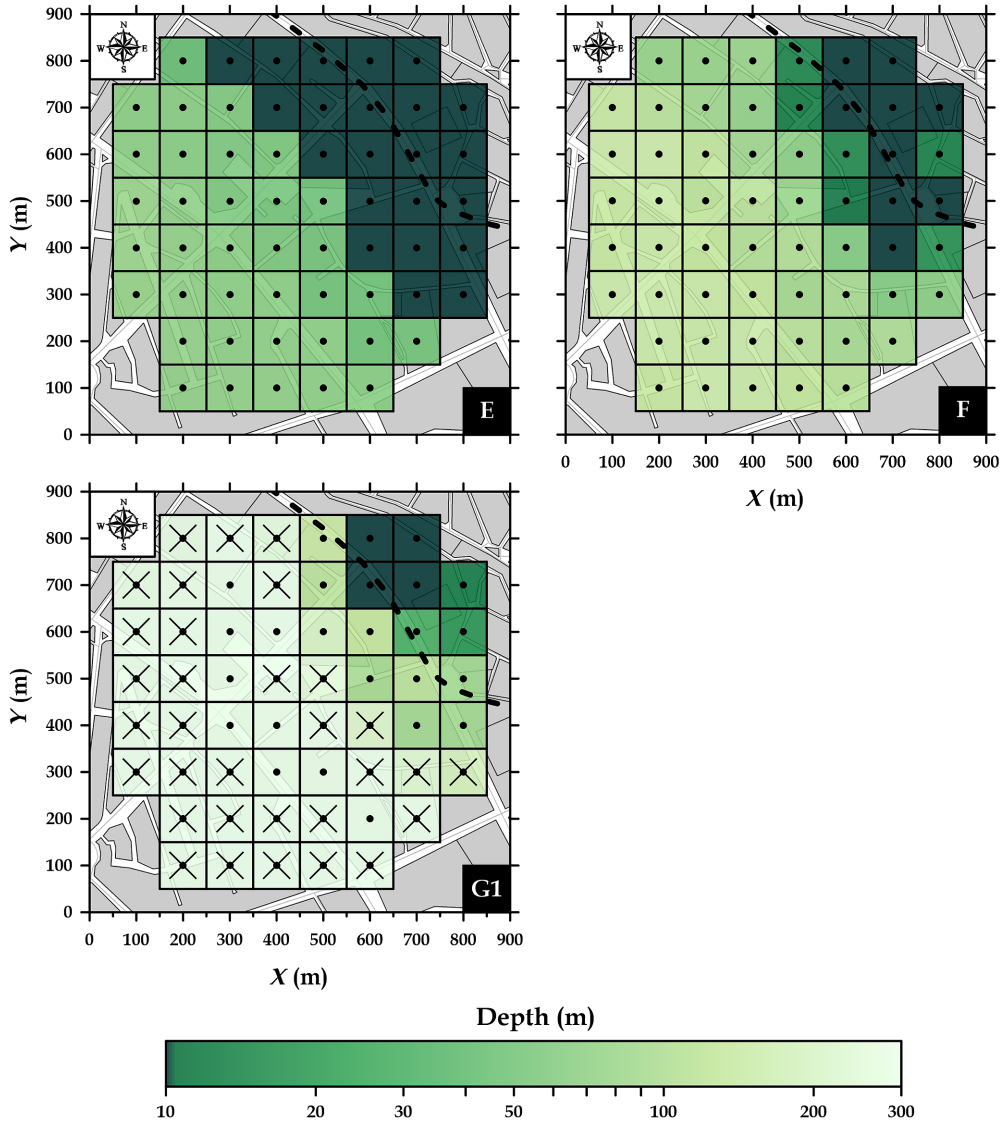

Figure 10. Final geophysical model showing the depth of the lower boundary for layers E, F, and G1 of Table 1. Tomographic grid nodes with depths ≤10 m (average minimum-depth resolution limit) and depths exceeding the maximum-depth resolution limit are depicted with dark colors and a cross symbol, respectively. The dashed line indicates the surface contact of bedrock formations and recent sediments. The color version of this figure is available only in the electronic edition.

Ibs-von Seht and Wohlenberg, 1999), whereas it is processing practically standardized (e.g., SESAME project; Bard, 2004). However, because our local structure (Table 1) involves two high-impedance contrast interfaces (E/F and F/G1), the direct application of a simplistic approach is questionable. To explore the HVSR usefulness, we compared the theoretical fundamental period, T_0, of the sedimentary cover in the examined area (as determined from the final V_S model of each node) with the corresponding value derived from the peak of the ambient noise HVSR curve, which has been shown to present an excellent correlation with the fundamental period (e.g., Haghshenas *et al.*, 2008) of a site. Because the T_0 values were available only for each recording station, we spatially interpolated the T_0 values from the HVSR curves to obtain an experimental ("observed") T_0 estimate at each tomographic grid node. For this evaluation, we considered two cases: (1) The local 1D V_S model up to (and including) the seismic bedrock (formation F in Table 1) and (2) the same model up to (and including) the gneiss bedrock (formation G1), in an attempt to identify the interface that is "responsible" for the observed fundamental peak in the HVSR curves.

The plot of the theoretical (from the local dispersion curves inverted V_S models) versus the experimental T_0 values (from the ambient noise HVSR curves), considering both bedrock (seismic—F and geological—G1) as the lower model layers, is presented in Figure 11. Two different patterns are seen in this figure, with nodes in the southwest part of the array (thick sediments area) exhibiting a clear linear correlation with the theoretical T_0 values. When the seismic bedrock is the lower model layer (E/F interface), the agreement with the HVSR data is much better in comparison to the results for the F/G1 interface (geological bedrock contact). On the contrary, in the northwest part of the model (bedrock area) the fundamental period obtained from the HVSR data seems to be controlled by the depth of the actual gneiss bedrock, as the corresponding fundamental period agreement seems to be slightly improved. Thus, for the bedrock area (northeast) where the thickness of the sedimentary cover is small, the T_0 is mainly affected from the geological bedrock depth (F/G1 interface), whereas for the sedimentary area (southwest) the seismic bedrock (E/F Interface) appears to control the ground response characteristics. This result verifies the rather complex subsurface structure, because the thickness increase of the sedimentary cover toward the southwest is having a significant impact to the estimated T_0 values.

In Figure 12 we present a 3D view (as seen from the southwest model part) of the seismic bedrock (E/F interface), in

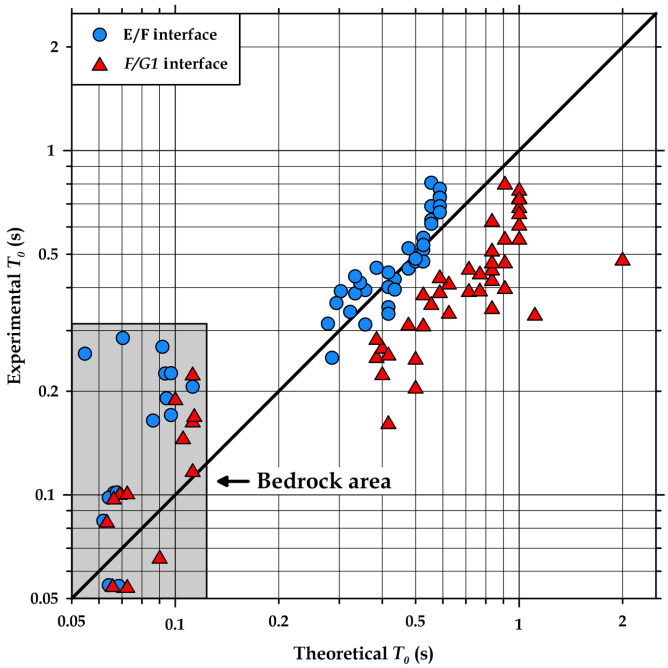

Figure 11. Comparison of theoretical and experimental T_0 values, derived from the recovered 1D V_S models of all grid nodes, as well as the application of the horizontal-to-vertical spectral ratio (HVSR) method on ambient noise recordings, respectively. Theoretical T_0 values were obtained by assuming the seismic bedrock (interface E/F, denoted with circles) as well as the geological bedrock (interface F/G1, denoted with triangles) as the model half-space. Data points in the bedrock area (northeast part of the study area) are included in the gray rectangle. The color version of this figure is available only in the electronic edition.

which the gradual dipping toward the southwest is evident. The interface shows a rather steep slope in the central part of the model, suggesting the presence of an inferred fault structure with a northwest–southeast strike, located close to the observed surface sediments–bedrock contact. This pattern is confirmed in Figure 13, which shows the averaged 2D model along the northeast–southwest cross section depicted in Figure 1. In this figure, we have also plotted the minimum and the maximum depth resolution limits, which suggest that we cannot recover the depths of the Holocene and Quaternary deposits (layers A and B), as well as the interbedrock transition (G1 to G) for depths larger than ~250 m in the southwest part of the study area (see also previous discussion for Figs. 9 and 10); however, interfaces E/F (seismic bedrock) and F/G1 (geological bedrock) of the subsurface geophysical structure are reliably recovered. Figure 13 also verifies the excellent correlation of surface geology and the final V_S model, with the bedrock–sediments contact being in good agreement with the location of the rapid increase of the thickness of layers E and F.

To further assess the new geophysical model, in comparison to the reference model of Anastasiadis *et al.* (2001), we present the geological bedrock depth (F/G1) in Figure 14, along the same northeast–southwest cross section used in Figure 13. Although the recovered bedrock depths are similar in both the models, the bedrock in the new model is closer to the surface in the northeast part of the study area, dipping much more steeply and to larger depths toward the southwest, hence, indicating the presence of a fault at distances of ~700–850 m along the profile, similar to the observation previously made in Figure 12 for the seismic bedrock.

CONCLUSIONS

In the present work, we examined the applicability of ambient noise array tomography for determining the near-surface 3D V_S structure at geotechnical scales (area of ~1 km^2, investigation depth ~200–300 m) of an urban area (city of Thessaloniki, Northern Greece). We employed several modifications over the previous standard implementations to handle the complex problems that arise in urban settings, such as approximate Fresnel volumes to account for the actual ray sensitivity area, interfrequency smoothing constraints to produce data-compatible smooth dispersion curves, and an iterative process to detect and reject travel time data outliers. Finally, we employed quantitative cutoff criteria to determine the robust and reliable part of the inverted dispersion curves, leading to their recovery within a spatially variable frequency content.

The ambient noise array tomography application at this scale and within a city complex revealed several aspects of the methodology that could be of interest for implementation at similar environments and spatial scales. For instance, the typical near-surface heterogeneities of the geological–geophysical structure in urban sites, often with the presence of artificial (human-made constructions) layers, can significantly affect the propagation of ambient noise. This fact, combined with the complicated noise source distribution in urban environments, results in a rather complex noise wavefield. As a result, asymmetries and incoherent signals are identified in the cross correlation traces, making the identification of surface wave travel times quite difficult. Thus, the calculation of the rms envelope amplitude of the multiple filter analysis plots from both negative and positive sections (Fig. 2c) facilitated the picking of dispersion curves for every path of the array and the extraction of Rayleigh wave travel times.

An interesting issue of the ambient noise tomography application concerns the spatial coherency of the finally inverted 1D V_S profiles. Although the reconstructed local group slowness dispersion curves are consistent within their neighborhood, due to the employed spatial smoothing constraints, the coherency of the inverted adjacent 1D V_S profiles cannot be easily controlled. The use of an appropriate ground model parameterization based on a priori information, as performed in this study, proved to be rather critical in allowing the recovery of a reliable, spatially coherent model, as shown in Figure 10.

Nevertheless, it should be noted that the very shallow part of the model is locally poorly constrained; to obtain accurate estimates of the uppermost structure would require a much denser

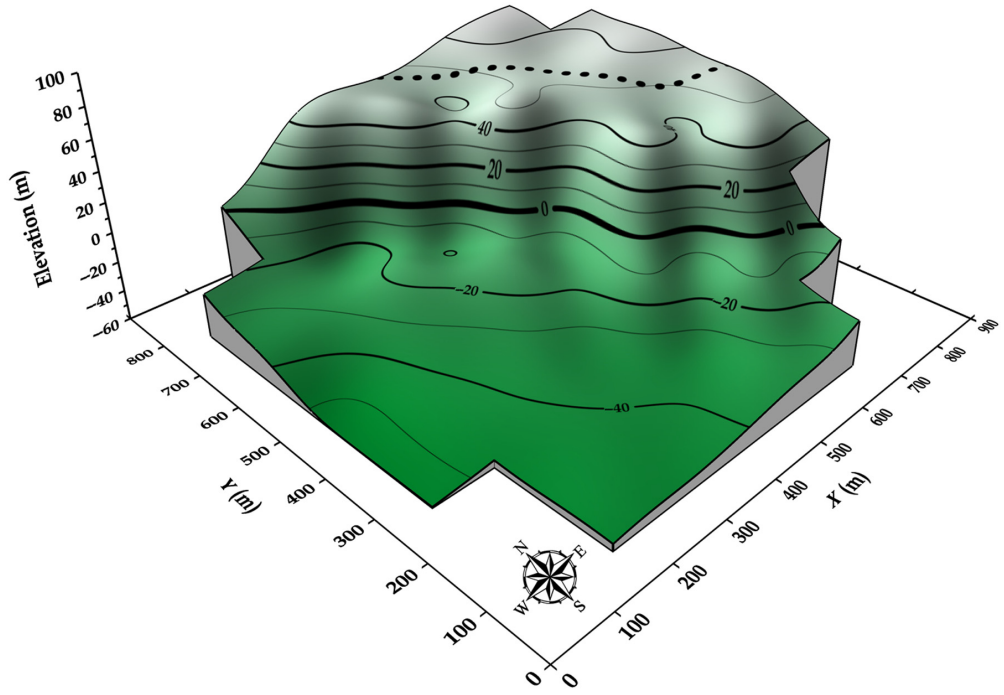

Figure 12. 3D view of the seismic bedrock elevation above sea level (E/F interface, vertical exaggeration of 2). The dashed line indicates the surface transition from bedrock formations to recent sediments. The color version of this figure is available only in the electronic edition.

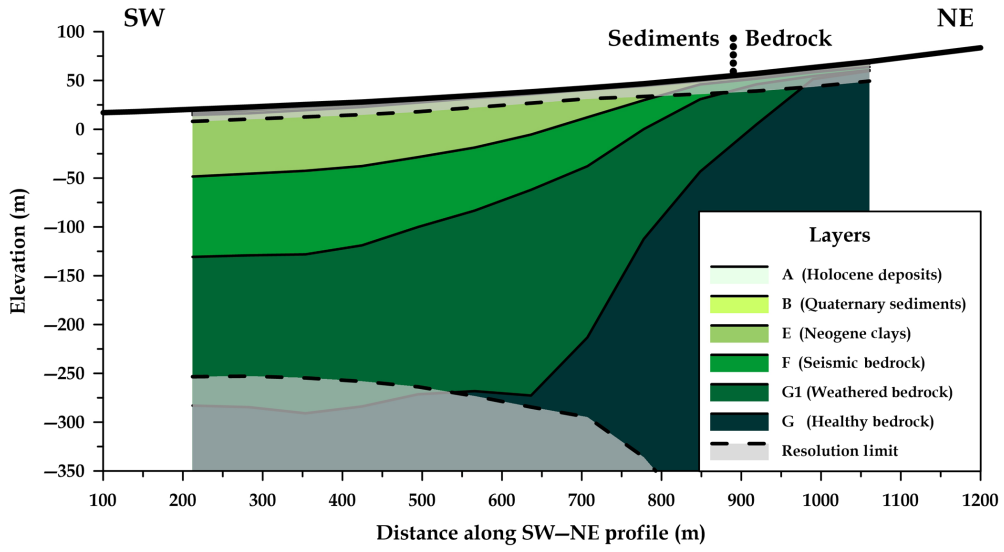

Figure 13. Average 2D structure along the southwest–northeast cross section shown in Figure 1a. The dashed lines depict the depth resolution limits. The surface geology sediments–bedrock transition contact is also indicated with a dotted vertical line. The color version of this figure is available only in the electronic edition.

network that could record higher frequency (smaller wavelengths) of ambient noise with increased spatial resolution. Especially in sedimentary basins, such as in our case, the scarcity of high frequency data is more profound due to the attenuation of the surface waves propagating through thick sediment formations. Moreover, the inability to record very low frequencies (<1.5 Hz), despite using broadband sensors, has limited the maximum resolving depth in the southwest part of the model (largest sediment thickness area) to ~250–300 m, not allowing us to reliably constrain any inter-bedrock velocity increase.

Despite the previously mentioned limitations, the proposed 3D geophysical model from the ambient noise tomography can be considered as both reliable and informative. Its general features are compatible with the available geological, geophysical, and geotechnical data for the study area, for example, verifying the rather 2D character of the subsurface structure (see Fig. 10), and suggest similar values for the bedrock depth (see Fig. 14). However, it also provides additional information not available in the previous, rather smooth, reference models. More specifically, the seismic (Fig. 12) and geological bedrock morphology (Figs. 10, 14) suggest the possible presence of a northwest–southeast-trending fault structure in the study area, which is even identified in the original group velocity maps (Fig. 6), in excellent agreement with the surface sediments–bedrock contact. We should point out that the geometry of the seismic bedrock (E/F interface) was very robust in all the model parameterizations we tested, showing that the employed dataset can efficiently resolve such formations that are usually of special interest for practical applications (e.g., site effect assessment on strong ground motions).

This study suggests that the implementation of ambient noise tomography is not only feasible but that it can also

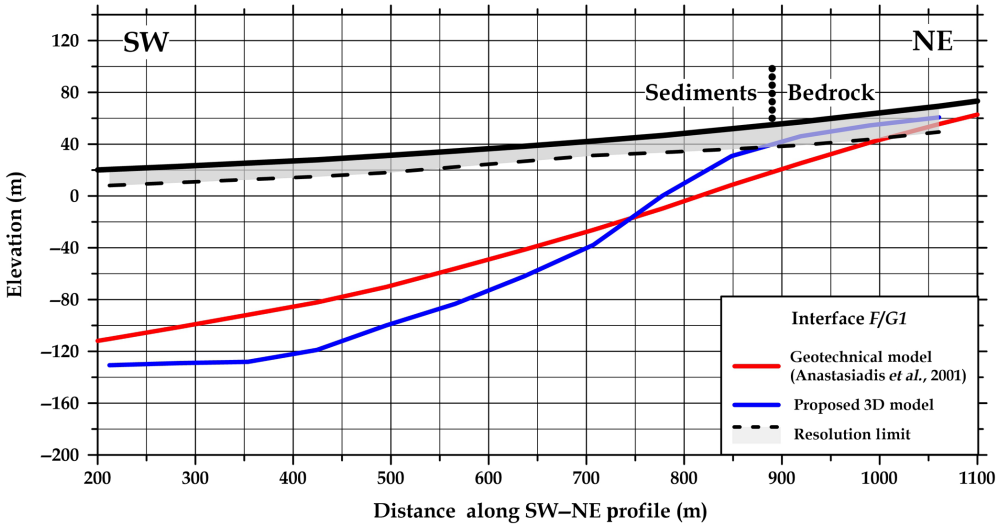

Figure 14. Comparison of the depth variation for the seismic bedrock (interface F/G1) from the updated 3D geophysical structure model and the geotechnical model of Anastasiadis *et al.* (2001) along a southwest–northeast profile in the study area (see Fig. 1a). The dashed line indicates the lower depth resolution limit, whereas the dotted vertical line depicts the surface contact of the bedrock with the recent sedimentary deposits. The color version of this figure is available only in the electronic edition.

efficiently contribute to a variety of practical applications in urban environments. The main drawback of the application appears to be its multistep nature, with several parameters requiring a user intervention (dispersion curve and uncertainty picking, regularization of travel time inversion, setup of the model parametric space, etc.), implying that its application cannot (yet) be fully automated. It is possible that the use of additional data or constraints could facilitate the method's application. Such data could incorporate information extracted from the ambient noise wavefield (radial and transverse component cross correlations to extract alternative Rayleigh and Love wave dispersion curves, joint inversions with Rayleigh-wave ellipticity, or HVSR curves, etc.) from earthquake records (e.g., joint inversion of dispersion curves and transfer functions) or independent information (e.g., constraints provided from other geological, geophysical, and geotechnical data, such as local downhole or crosshole V_S profile, estimates of bedrock depth from boreholes, etc.). It should be noted that the derived 3D V_S model could facilitate additional research work in this direction, such as 3D numerical modeling to determine the local HVSR curves, without relying on 1D assumptions. The previous information, combined with different approaches for the data processing and inversion (e.g., incorporation of phase velocities, especially from denser arrays), could facilitate the semiautomatic implementation of ambient noise tomography in urban environments and engineering scale projects.

DATA AND RESOURCES

Data employed in this study were collected with instruments from the inventory of the Geophysical Laboratory, Aristotle University Thessaloniki, and the Institute of Engineering Seismology and Earthquake Engineering (ITSAK) and can be available upon request. Some plots were made using the Generic Mapping Tools version 4.2.1 (https://www.soest.hawaii.edu/gmt, last accessed January 2020; Wessel and Smith, 1998).

DECLARATION OF COMPETING INTERESTS

The authors acknowledge that there are no conflicts of interest recorded.

ACKNOWLEDGMENTS

The research project was supported by the Hellenic Foundation for Research and Innovation (H.F.R.I.) under the "First Call for H.F.R.I. research projects to support faculty members and researchers, and the procurement of high-cost research equipment grant" (Project Protectant, Number 2924). The authors would like to thank Thomas Pratt and all the anonymous reviewers that provided useful comments and constructive criticism, helping to improve the content of our work.

REFERENCES

Aki, K. (1957). Space and time spectra of stationary stochastic waves, with special reference to microtremors, *Bull. Earthq. Res. Inst.* **35,** 415–457.

Aki, K., and W. H. K. Lee (1976). Determination of three-dimensional velocity anomalies under a seismic array using first P arrival times from local earthquakes, 1. A homogeneous initial model, *J. Geophys. Res.* **81,** 4381–4399.

Anastasiadis, A., D. Raptakis, and K. Pitilakis (2001). Thessaloniki's detailed microzoning: Subsurface structure as basis for site response analysis, *Pure Appl. Geophys.* **158,** 2597–2633.

Anthymidis, M., N. Theodoulidis, A. Savvaidis, and C. Papazachos (2012). Constraining site response and shallow geophysical structure by ambient noise measurements and 1D numerical simulations: The case of Grevena town (N. Greece), *Bull. Earthq. Eng.* **10,** 1685–1716.

Apostolidis, P., D. Raptakis, Z. Roumelioti, and K. Pitilakis (2004). Determination of S-wave velocity structure using microtremors and SPAC method applied in Thessaloniki (Greece), *Soil Dynam. Earthq. Eng.* **24,** 49–67.

Asano, K., T. Iwata, H. Sekiguchi, K. Somei, K. Miyakoshi, S. Aoi, and T. Kunugi (2017). Surface wave group velocity in the Osaka sedimentary basin, Japan, estimated using ambient noise cross-correlation functions, *Earth Planets Space* **69,** doi: 10.1186/s40623-017-0694-3.

Athanasiou, E. (2004). Development of algorithms for the optimal strategic measurement and inversion of electric tomography data, *Ph.D. Thesis*, Aristotle University of Thessaloniki, Greece, 168 pp.

Bard, P.-Y., and M. Bouchon (1985). The two-dimensional resonance of sediment-filled valleys, *Bull. Seismol. Soc. Am.* **75,** 519–541.

Bard, P.-Y., and SESAME Participants (2004). The SESAME project: An overview and main results, *13th World Conf. on Earthquake Engineering*, Vancouver, B.C., Canada.

Bensen, G. D., M. H. Ritzwoller, M. P. Barmin, A. L. Levshin, F. Lin, M. P. Moschetti, N. M. Shapiro, and Y. Yang (2007). Processing seismic ambient noise data to obtain reliable broad-band surface wave dispersion measurements, *Geophys. J. Int.* **169,** 1239–1260.

Bonnefoy-Claudet, S., F. Cotton, and P.-Y. Bard (2006). The nature of noise wavefield and its applications for site effects studies. A literature review, *Earth Sci. Rev.* **79,** 205–227.

Campillo, M., and A. Paul (2003). Long range correlations in the diffuse seismic coda, *Science* **299,** 547–549.

Capon, J. (1969). High-resolution frequency-wavenumber spectrum analysis, *Proc. IEEE* **57,** 146–156.

Cárdenas-Soto, M., D. Escobedo-Zenil, A. Tejero-Andrade, M. Nava-Flores, M. Vidal-García, and T. Natarajan (2020). Exploring a near-surface subsidence over a rehabilitated underground mine through ambient seismic noise tomography in combination with other geophysical methods, *Near Surf. Geophys.* **18,** 483–495.

Cerveny, V., and J. E. P. Soares (1992). Fresnel volume ray tracing, *Geophysics* **57,** 902–915.

Chávez-García, F. J., and P.-Y. Bard (1994). Site effects in Mexico City eight years after the September 1985 Michoacan earthquakes, *Soil Dynam. Earthq. Eng.* **13,** 229–247.

Chávez-García, F. J., and F. Luzon (2005). On the correlation of seismic microtremors, *J. Geophys. Res.* **110,** no. B11, doi: 10.1029/2005JB003671.

Chávez-García, F. J., M. Rodríguez, and W. R. Stephenson (2005). An alternative approach to the SPAC analysis of microtremors: Exploiting stationarity of noise, *Bull. Seismol. Soc. Am.* **95,** 277–293.

Clayton, R., P. Persaud, M. Denolle, and J. Polet (2019). Exposing Los Angeles's shaky geologic underbelly, *Eos Trans. AGU* **100,** doi: 10.1029/2019EO135099.

Constable, S. C., R. L. Parker, and C. G. Constable (1987). Occam's inversion: A practical algorithm for generating smooth models from electromagnetic sounding data, *Geophysics* **52,** 289–300.

Cornou, C., M. Ohrnberger, D. Boore, D. Kudo, and P.-Y. Bard (2006). Derivation of structural models from ambient vibration array recordings: Results from an international blind test, *Proc. of the 3rd Int. Symp. Effects Surf. Geol. Seism. Motion*.

Curtis, A., P. Gerstoft, H. Sato, R. Snieder, and K. Wapenaar (2006). Seismic interferometry—Turning noise into signal, *The Leading Edge* **25,** 1082–1092.

Czarny, R., Z. Pilecki, N. Nakata, E. Pilecka, K. Krawiec, P. Harba, and M. Barnaś (2019). 3D S-wave velocity imaging of a subsurface disturbed by mining using ambient seismic noise, *Eng. Geol.* **251,** 115–127.

Derode, A., E. Larose, M. Campillo, and M. Fink (2003). How to estimate the Green's function of a heterogeneous medium between two passive sensors? Application to acoustic waves, *Appl. Phys. Lett.* **83,** 3054–3056.

Di Giulio, G., C. Cornou, M. Ohrnberger, M. Wathelet, and A. Rovelli (2006). Deriving wavefield characteristics and shear-velocity profiles from two-dimensional small-aperture arrays analysis of ambient vibrations in a small-size alluvial basin, Colfiorito, Italy, *Bull. Seismol. Soc. Am.* **96,** 1915–1933.

Di Giulio, G., A. Savvaidis, M. Ohrnberger, M. Wathelet, C. Cornou, B. Knapmeyer-Endrun, F. Renalier, N. Theodoulidis, and P.-Y. Bard (2012). Exploring the model space and ranking a best class of models in surface-wave dispersion inversion: Application at European strong-motion sites, *Geophysics* **77,** 147–166.

Dziewonski, A., S. Bloch, and M. Landisman (1969). A technique for the analysis of transient seismic signals, *Bull. Seismol. Soc. Am.* **59** 427–444.

Foti, S., F. Hollender, F. Garofalo, D. Albarello, M. Asten, P.-Y. Bard, C. Comina, C. Cornou, B.R. Cox, G. Di Giulio, *et al.* (2017). Guidelines for the good practice of surface wave analysis: A product of the InterPACIFIC project, *Bull. Earthq. Eng.* **16,** 2367–2420.

Franklin, J. N. (1970). Well-posed stochastic extensions of ill-posed linear problems, *J. Math. Anal. Appl.* **31,** 682–716.

García-Jerez, A., F. Luzón, M. Navarro, and M. A. Santoyo (2010). Assessing the reliability of the single circular-array method for Love-wave ambient-noise surveying, *Bull. Seismol. Soc. Am.* **100,** 2230–2249.

Garofalo, F., S. Foti, F. Hollender, P.-Y. Bard, C. Cornou, B. R. Cox, M. Ohrnberger, D. Sicilia, M. Asten, G. Di Giulio, *et al.* (2016). InterPACIFIC project: Comparison of invasive and non-invasive methods for seismic site characterization. Part I: Intra-comparison of surface wave methods, *Soil Dynam. Earthq. Eng.* **82,** 222–240.

Gouédard, P., C. Cornou, and P. Roux (2008). Phase-velocity dispersion curves and small-scale geophysics using noise correlation slantstack technique, *Geophys. J. Int.* **172,** 971–981.

Gouédard, P., L. Stehly, F. Brenguier, M. Campillo, Y. Colin De Verdière, E. Larose, L. Margerin, P. Roux, F. J. Sánchez-Sesma, N. M. Shapiro, *et al.* (2008). Cross-correlation of random fields: Mathematical approach and applications, *Geophys. Prospect.* **56,** 375–393.

Goutorbe, B., D. L. de Oliveira Coelho, and S. Drouet (2015). Rayleigh wave group velocities at periods of 6-23 s across Brazil from ambient noise tomography, *Geophys. J. Int.* **203,** 869–882.

Haghshenas, E., P.-Y. Bard, and N. Theodulidis (2008). Empirical evaluation of microtremor H/V spectral ratio, *Bull. Earthq. Eng.* **6,** 75–108.

Hannemann, K., C. Papazachos, M. Ohrnberger, A. Savvaidis, M. Anthymidis, and A. M. Lontsi (2014). Three-dimensional shallow structure from high-frequency ambient noise tomography: New results for the Mygdonia basin-Euroseistest area, northern Greece, *J. Geophys. Res.* **119,** 4979–4999.

Hollender, F., C. Cornou, A. Dechamp, K. Oghalaei, F. Renalier, E. Maufroy, C. Burnouf, S. Thomassin, M. Wathelet, and P.-Y. Bard (2017). Characterization of site conditions (soil class, VS30, velocity profiles) for 33 stations from the French permanent accelerometric network (RAP) using surface-wave methods, *Bull. Earthq. Eng.* **16,** 2337–2365.

Huang, Y. C., T. Ohkura, T. Kagiyama, S. Yoshikawa, and H. Inoue (2018). Shallow volcanic reservoirs and pathways beneath Aso caldera revealed using ambient seismic noise tomography, *Earth Planets Space* **70,** doi: 10.1186/s40623-018-0941-2.

Huang, Y. C., H. Yao, B.-S. Huang, R. D. van der Hilst, K.-L. Wen, W.-G. Huang, and C.-H. Chen (2010). Phase velocity variation at periods of 0.5–3 seconds in the Taipei basin of Taiwan from

correlation of ambient seismic noise, *Bull. Seismol. Soc. Am.* **100,** 2250–2263.

Ibs-von Seht, M., and J. Wohlenberg (1999). Microtremor measurements used to map thickness of soft sediments, *Bull. Seismol. Soc. Am.* **89,** 250–259.

Inbal, A., J. P. Ampuero, and R. W. Clayton (2016). Localized seismic deformation in the upper mantle revealed by dense seismic arrays, *Science* **354,** 88–92.

Inzunza, D. A., G. A. Montalva, F. Leyton, G. Prieto, and S. Ruiz (2018). Shallow ambient-noise 3D tomography in the concepción basin, Chile: Implications for low-frequency ground motions, *Bull. Seismol. Soc. Am.* **109,** 75–86.

Jackson, D. D. (1979). The use of a priori data to resolve non-uniqueness in linear inversion, *Geophys. J. Roy. Astron. Soc.* **57,** 137–157.

Kao, H., Y. Behr, C. A. Currie, R. Hyndman, J. Townend, F. Lin, M. H. Ritzwoller, S. J. Shan, and J. He (2013). Ambient seismic noise tomography of Canada and adjacent regions: Part I. Crustal structures, *J. Geophys. Res.* **118,** 5865–5887.

Köhler, A., M. Ohrnberger, F. Scherbaum, M. Wathelet, and C. Cornou (2007). Assessing the reliability of the modified three-component spatial autocorrelation technique, *Geophys. J. Int.* **168,** 779–796.

Kugler, S., T. Bohlen, T. Forbriger, S. Bussat, and G. Klein (2007). Scholtewave tomography for shallow-water marine sediments, *Geophys. J. Int.* **168,** 551–570.

Lacoss, R. T., E. J. Kelly, and M. N. Toksöz (1969). Estimation of seismic noise structure using arrays, *Geophysics* **34,** 21–38.

Larose, E., A. Derode, M. Campillo, and M. Fink (2004). Imaging from one-bit correlations of wideband diffuse wave fields, *J. Appl. Phys.* **95,** 8393–8399.

Lehujeur, M., J. Vergne, J. Schmittbuhl, and A. Maggi (2015). Characterization of ambient seismic noise near a deep geothermal reservoir and implications for interferometric methods: A case study in northern Alsace, France, *Geotherm. Energy* **3,** doi: 10.1186/s40517-014-0020-2.

Liang, F., Z. Wang, H. Li, K. Liu, and T. Wang (2019). Near-surface structure of downtown Jinan, China: Application of ambient noise tomography with a dense seismic array, *J. Env. Eng. Geophys.* **24,** 641–652.

Lin, F. C., D. Li, R. W. Clayton, and D. Hollis (2013). High-resolution 3D shallow crustal structure in Long Beach, California: Application of ambient noise tomography on a dense seismic array, *Geophysics* **78,** 45–56.

Lin, F. C., M. H. Ritzwoller, J. Townend, S. Bannister, and M. K. Savage (2007). Ambient noise Rayleigh wave tomography of New Zealand, *Geophys. J. Int.* **170,** 649–666.

Liu, G., P. Persaud, and R. W. Clayton (2018). Structure of the northern Los Angeles basins revealed in teleseismic receiver functions from short-term nodal seismic arrays, *Seismol. Res. Lett.* **89,** 1680–1689.

Lobkis, O. I., and R. L. Weaver (2001). On the emergence of the Green's function in the correlations of a diffuse field, *J. Acoust. Soc. Am.* **110,** 3011–3017.

Lontsi, A. M., M. Ohrnberger, and F. Krüger (2016). Shear wave velocity profile estimation by integrated analysis of active and passive seismic data from small aperture arrays, *J. Appl. Geophys.* **130,** 37–52.

Louie, J. (2001). Faster, better: Shear-wave velocity to 100 meters depth from refraction microtremor arrays, *Bull. Seismol. Soc. Am.* **91,** 347–364.

Ma, Y., and R. W. Clayton (2016). Structure of the Los Angeles basin from ambient noise and receiver functions, *Geophys. J. Int.* **206,** 1645–1651.

Malcolm, A. E., J. A. Scales, and B. A. van Tiggelen (2004). Extracting the Green function from diffuse, equipartitioned waves, *Phys. Rev. E* **70,** doi: 10.1103/PhysRevE.70.015601.

Martínez-Pagán, P., M. Navarro, J. Pérez-Cuevas, F. J. Alcalá, A. García-Jerez, and F. Vidal (2018). Shear-wave velocity structure from MASW and SPAC methods: The case of Adra town, SE Spain, *Near Surf. Geophys.* **16,** 356–371.

Michelini, A., and T.V. McEvilly (1991). Seismological studies at Parkfield. I. Simultaneous inversion for velocity structure and hypocenters using cubic B-splines parameterization, *Bull. Seismol. Soc. Am.* **81,** 524–552.

Mulargia, F. (2012). The seismic noise wavefield is not diffuse, *J. Acoust. Soc. Am.* **131,** 2853–2858.

Nakamura, Y. (1989). A method for dynamic characteristics estimation of subsurface using microtremor on the ground surface, *Q. Rep. Railway Tech. Res. Inst.* **30,** 25–33.

Nakata, N., R. Snieder, T. Tsuji, K. Larner, and T. Matsuoka (2011). Shear wave imaging from traffic noise using seismic interferometry by cross-coherence, *Geophysics* **76,** 97–106.

Nunziata, C., G. De Nisco, and G. F. Panza (2009). S-waves profiles from noise cross correlation at small scale, *Eng. Geol.* **105,** 161–170.

Obermann, A., T. Kraft, E. Larose, and S. Wiemer (2015), Potential of ambient seismic noise techniques to monitor the St. Gallen geothermal site (Switzerland), *J. Geophys. Res.* **120,** 4301–4316.

Obermann, A., M. Lupi, A. Mordret, S. S. Jakobsdóttir, and S. A. Miller (2016). 3D-ambient noise Rayleigh wave tomography of Snæfellsjökull volcano, Iceland, *J. Volcanol. Geotherm. Res.* **317,** 42–52.

Ohrnberger, M., E. Schissele, C. Cornou, S. Bonnefoy-Claudet, M. Wathelet, A. Savvaidis, F. Scherbaum, and D. Jongmans (2004). Frequency wavenumber and spatial autocorrelation methods for dispersion curve determination from ambient vibration recordings, *13th World Conf. on Earthquake Eng.*

Oikonomou, D. (2017). Contribution to the combined application of seismic and geoelectric tomographic methods, *Master's Thesis*, Aristotle University of Thessaloniki, Greece, 172 pp.

Panou, A., N. Theodulidis, P. Hatzidimitriou, K. Stylianidis, and C. Papazachos (2005). Ambient noise horizontal-to-vertical spectral ratio in site effects estimation and correlation with seismic damage distribution in urban environment: The case of the city of Thessaloniki (Northern Greece), *Soil Dynam. Earthq. Eng.* **25,** 261–274.

Papadopoulos, I., C. Papazachos, A. Savvaidis, N. Theodoulidis, and F. Vallianatos (2017). Seismic microzonation of the broader Chania basin area (southern Greece) from the joint evaluation of ambient noise and earthquake recordings, *Bull. Earthq. Eng.* **15,** 861–888.

Pastén, C., M. Sáez, S. Ruiz, F. Leyton, J. Salomón, and P. Poli (2016). Deep characterization of the Santiago basin using HVSR and cross-correlation of ambient seismic noise, *Eng. Geol.* **201,** 57–66.

Pelekis, P. C., and G. A. Athanasopoulos (2011). An overview of surface wave methods and a reliability study of a simplified inversion technique, *Soil Dynam. Earthq. Eng.* **12,** 1654–1668.

Picozzi, M., S. Parolai, D. Bindi, and A. Strollo (2009). Characterization of shallow geology by high-frequency seismic noise tomography, *Geophys. J. Int.* **176,** 164–174.

Pilz, M., and S. Parolai (2014). Statistical properties of the seismic noise field: Influence of soil heterogeneities, *Geophys. J. Int.* **199,** 430–440.

Pilz, M., S. Parolai, M. Picozzi, and D. Bindi (2012). Three-dimensional shear wave velocity imaging by ambient seismic noise tomography, *Geophys. J. Int.* **189,** 501–512.

Planès, T., A. Obermann, V. Antunes, and M. Lupi (2020). Ambient-noise tomography of the Greater Geneva Basin in a geothermal exploration context, *Geophys. J. Int.* **220,** 370–383.

Renalier, F., D. Jongmans, M. Campillo, and P.-Y. Bard (2010). Shear wave velocity imaging of the Avignonet landslide (France) using ambient noise cross correlation, *J. Geophys. Res.* **115,** doi: 10.1029/2009JF001538.

Roux, P., K. G. Sabra, W. A. Kuperman, and A. Roux (2005). Ambient noise cross correlation in free space: Theoretical approach, *J. Acoust. Soc. Am.* **117,** 79–84.

Sager, K., L. Ermert, C. Boehm, and A. Fichtner (2018). Towards full waveform ambient noise inversion, *Geophys. J. Int.* **212,** 566–590.

Sambridge, M. (1999a). Geophysical inversion with a neighbourhood algorithm—I. Searching a parameter space, *Geophys. J. Int.* **138,** 479–494.

Sambridge, M. (1999b). Geophysical inversion with a neighbourhood algorithm—II. Appraising the ensemble, *Geophys. J. Int.* **138,** 727–746.

Saygin, E., and B. L. N. Kennett (2010). Ambient seismic noise tomography of Australian continent, *Tectonophysics* **481,** 116–125.

SESAME European Research Project (2004). Guidelines for the implementation of the H/V spectral ratio technique on ambient vibrations: Measurements, processing, and interpretation, *WP12—Deliverable D23.12*.

Shapiro, N. M., and M. Campillo (2004). Emergence of broadband Rayleigh waves from correlations of the ambient seismic noise, *Geophys. Res. Lett.* **31,** 8–11.

Shapiro, N., M. Campillo, L. Stehly, and M. H. Ritzwoller (2005). High-resolution surface-wave tomography from ambient seismic noise, *Science* **307,** 1615–1618.

Skarlatoudis, A., C. Papazachos, N. Theodoulidis, J. Kristek, and P. Moczo (2010). Local site-effects for the city of Thessaloniki (N. Greece) using a 3-D finite-difference method: A case of complex dependence on source and model parameters, *Geophys. J. Int.* **182,** 279–298.

Snieder, R. (2004). Extracting the Green's function from the correlation of coda waves: A derivation based on stationary phase, *Phys. Rev. E* **69,** doi: 10.1103/PhysRevE.69.046610.

Soupios, P., C. Papazachos, C. Juhlin, and G. Tsokas (2001). Nonlinear 3-D traveltime inversion of crosshole data with an application in the area of the Middle Ural mountains, *Geophysics* **66,** 627–636.

Stehly, L., M. Campillo, and N. M. Shapiro (2006). A study of the seismic noise from its long-range correlation properties, *J. Geophys. Res.* **111,** doi: 10.1029/2005JB004237.

Taylor, G., S. Rost, G. Houseman, and G. Hillers (2019). Near-surface structure of the north Anatolian fault zone from Rayleigh and Love wave tomography using ambient seismic noise, *Solid Earth* **10,** 363–378.

Tokimatsu, K. (1995). Geotechnical site characterization using surface waves, *Proc. of the 1st Int. Conf. on Earthquake Geotech. Eng.*, 1333–1368.

Toomey, D. R., and G. R. Foulger (1989). Tomographic inversion of local earthquake data from the Hengill-Grensdalur central volcano complex, Iceland, *J. Geophys. Res.* **94,** 17,497–17,510.

Wapenaar, K., J. Thorbecke, and D. Draganov (2004). Relations between reflection and transmission responses of three-dimensional inhomogeneous media, *Geophys. J. Int.* **156,** 179–194.

Wathelet, M. (2008). An improved neighborhood algorithm: Parameter conditions and dynamic scaling, *Geophys. Res. Lett.* **35,** doi: 10.1029/2008GL033256.

Wathelet, M., J.-L. Chatelain, C. Cornou, G. Di Giulio, B. Guillier, M. Ohrnberger, and A. Savvaidis (2020). Geopsy: A user-friendly open-source tool set for ambient vibration processing, *Seismol. Res. Lett.* **91,** 1878–1889.

Wathelet, M., D. Jongmans, M. Ohrnberger, and S. Bonnefoy-Claudet (2008). Array performances for ambient vibrations on a shallow structure and consequences over Vs inversion, *J. Seismol.* **12,** 1–19.

Weaver, R. L., and O. I. Lobkis (2004). Diffuse fields in open systems and the emergence of the Green's function (L), *J. Acoust. Soc. Am.* **116,** 2731–2734.

Wessel, P., and W. H. F. Smith (1998). New, improved version of the generic mapping tools released, *Eos Trans. AGU* **79,** 579.

Xu, H., Y. Luo, C. Chen, and Y. Xu (2016). 3D shallow structures in the Baogutu area, Karamay, determined by eikonal tomography of short-period ambient noise surface waves, *J. Appl. Geophys.* **129,** 101–110.

Xu, Z., T. Mikesell, J. Xia, and F. Cheng (2017). A comprehensive comparison between the refraction microtremor and seismic interferometry methods for phase-velocity estimation, *Geophysics* **82,** 99–108.

Yang, L., X. Liu, and G. C. Beroza (2021). Revisiting evidence for widespread seismicity in the upper mantle under Los Angeles, *Sci. Adv.* **7,** doi: 10.1126/sciadv.abf2862.

Yang, Y., M. H. Ritzwoller, A. L. Levshin, and N. M. Shapiro (2007). Ambient noise Rayleigh wave tomography across Europe, *Geophys. J. Int.* **168,** 259–274.

Zervopoulou, A. (2010). Neotectonic faults of the wide area of Thessaloniki in association with foundation soils, *Ph.D. Thesis*, Aristotle University of Thessaloniki, Greece, 300 pp.

Zhang, Y., Y. Li, H. Zhang, and T. Ku (2019). Near-surface site investigation by seismic interferometry using urban traffic noise in Singapore, *Geophysics* **84,** 169–180.

Zheng, L., X. Fan, P. Zhang, J. Hao, H. Qian, and T. Zheng (2021). Detection of urban hidden faults using group-velocity ambient noise tomography beneath Zhenjiang area, China, *Sci. Rep.* **11,** doi: 10.1038/s41598-020-80249-6.

Zhou, C., J. Xia, H. Zhang, J. Pang, Y. Liu, C. Xi, L. Ning, B. Mi, H. Xing, and X. Chang (2021). Urban near-surface imaging from ambient noise tomography using dense seismic networks, *9th Int. Conf. on Environmental Eng. Geophys.*

Manuscript received 10 January 2022
Published online 16 August 2022